doi:10.26443/seismica.v3i1.1186

SEISMICA

Mapping fault geomorphology with drone-based lidar

Guy Salomon * [1], **Theron Finley** [1], **Edwin Nissen** [1], **Roger Stephen** [1,2], **Brian Menounos** [3,4]

[1]School of Earth and Ocean Sciences, University of Victoria, Victoria, British Columbia, Canada, [2]Department of Geography, University of Victoria, Victoria, British Columbia, Canada, [3]Department of Geography, Earth, and Environmental Sciences, University of Northern British Columbia, Prince George, British Columbia, Canada, [4]Geological Survey of Canada, PO Box 6000, Sidney, BC V8L 4B2, Canada

Author contributions: *Conceptualization*: E.N., G.S., T.F. *Methodology*: G.S., R.S. *Formal Analysis*: G.S. *Investigation*: G.S., T.F., R.S., E.N., B.M. *Writing - original draft*: G.S.. *Writing - Review & Editing*: E.N., T.F, B.M. *Funding acquisition*: E.N., T.F., B.M.

Production Editor:
Gareth Funning
Handling Editor:
Randolph Williams
Copy & Layout Editor:
Oliver Lamb

Received:
January 18, 2024
Accepted:
May 5, 2024
Published:
June 3, 2024

Abstract The advent of sub-meter resolution topographic surveying has revolutionized active fault mapping. Light detection and ranging (lidar) data collected using crewed airborne laser scanning (ALS) can provide ground coverage of entire fault systems but is expensive, while Structure-from-Motion (SfM) photogrammetry from uncrewed aerial vehicles (UAVs) is popular for mapping smaller sites but cannot image beneath vegetation. Here, we present a new UAV laser scanning (ULS) system that overcomes these limitations to survey fault-related topography cost-effectively, at desirable spatial resolutions, and even beneath dense vegetation. In describing our system, data acquisition and processing workflows, we provide a practical guide for other researchers interested in developing their own ULS capabilities. We showcase ULS data collected over faults from a variety of terrain and vegetation types across the Canadian Cordillera and compare them to conventional ALS and SfM data. Due to the lower, slower UAV flights, ULS offers improved ground return density (∼260 points/m^2 for the capture of a paleoseismic trenching site and ∼10–72 points/m^2 for larger, multi-kilometer fault surveys) over conventional ALS (∼3–9 points/m^2) as well as better vegetation penetration than both ALS and SfM. The resulting ∼20–50 cm-resolution ULS terrain models reveal fine-scale tectonic landforms that would otherwise be challenging to image.

Non-technical summary Lidar remote sensing uses light pulses from a laser instrument to measure distances to objects and surfaces to create high precision, three-dimensional models. It is useful for mapping the ground surface where obscured by forest, because laser pulses that avoid foliage and branches will sample the ground surface while those that don't can be digitally removed, unlike in photogrammetry. Typically, lidar instruments are mounted on tripods (terrestrial laser scanning) or crewed aircraft (airborne laser scanning). Recently, lidar systems have become compact and light enough to be deployed from uncrewed aerial vehicles (UAVs, or drones) and this technology is being adopted across many disciplines. Here, we describe some of the first applications of a drone lidar system to study landforms generated by active faults, and illustrate its capabilities using surveys of a variety of faulted landscapes with different vegetation types across western Canada. Our system offers a cost-effective way of obtaining otherwise expensive lidar data, and compares favourably against established methods of topographic mapping, allowing us to survey the landscape in finer detail than was previously possible. The drone system is subject to practical and regulatory constraints and we discuss ways that these could be mitigated in the future.

1 Introduction

Lidar (light detection and ranging) is an increasingly popular terrestrial remote sensing method that combines the return times of reflected or back-scattered laser pulses with information on the location and orientation of the laser scanner to produce a dense 'point cloud' containing the Cartesian (x, y and z) co-ordinates of a geographic target (Xiaoye Liu, 2008; Glennie et al., 2013). The sub-meter point spacings characteristic of lidar data are finer than the ∼1–10 meter pixel dimensions typical of modern satellite-derived digital elevation models (DEMs) (e.g. Morin et al., 2016; Hodge et al., 2019; Wang et al., 2019; Benavente et al., 2021; Salomon et al., 2022). Furthermore, since multiple laser returns can be distinguished from the same outgoing pulse, and since distinct canopy returns can be filtered out, lidar is able to penetrate vegetation to yield a bare-earth digital terrain model (DTM) of the ground surface. These unique attributes of lidar remote sensing have contributed to an explosion of interest across many geospatial fields, including tectonic geomorphology (Meigs, 2013). It is becoming common practice to acquire lidar along fault surface traces as it provides some of the best data for constraining fault offsets, kinematics, and scarp morphology (e.g. Cunningham et al., 2006; Hilley et al., 2010; Zielke et al., 2010, 2015; Elliott et al., 2012; Salisbury et al., 2012; Johnson et al., 2018; Wei et al., 2019), as well as a topographic baseline for mapping any future earthquake deformation (Oskin et al., 2012; Glennie et al., 2014; Nissen et al., 2014; Scott et al., 2018; Diederichs et al., 2019; Ishimura et al., 2019; Lajoie et al., 2019; Wedmore et al., 2019) or aseismic fault

---

*Corresponding author: guysalomon@uvic.ca creep (DeLong et al., 2015; Scott et al., 2020). Lidar is especially useful in regions such as northwestern North America, where widespread forest cover may otherwise obscure fault scarps or other earthquake-related landforms (e.g. Haugerud et al., 2003; Hunter et al., 2011; Morell et al., 2017; Nelson et al., 2017; Johnson et al., 2018; Harrichhausen et al., 2021; Schermer et al., 2021; Witter et al., 2021).

Lidar data are typically collected through one of two established methods. In Terrestrial Laser Scanning (TLS), landscapes are mapped at low incidence angles from a laser instrument mounted on a stationary tripod (Telling et al., 2017). TLS can achieve very dense point clouds with 100s to 1000s of points per square meter (pts/m^2), but to avoid shadowing of features of interest behind objects like tree trunks or undulating topography, the scanner is typically deployed at several locations. Furthermore, due to the time taken to set up each new scanner position, TLS surveys are best suited for relatively small outcrop or landform-scale acquisitions (e.g. Jones et al., 2009; Haddad et al., 2012; Gold et al., 2013; Wiatr et al., 2013; Bubeck et al., 2015; DeLong et al., 2015; Wedmore et al., 2019). In rare instances, terrestrial lidar surveys have been expanded by mounting the scanner on motorized vehicles, backpacks, or tethered balloons, a configuration termed Mobile Laser Scanning (MLS) (Glennie et al., 2013; Brooks et al., 2013; Brooks et al., 2017; Nevitt et al., 2020; Zhu et al., 2022). The second, more prevalent method is Airborne Laser Scanning (ALS), where the laser scanner is mounted onto a crewed aircraft and flown over the target area (Xiaoye Liu, 2008; Glennie et al., 2013). This method is suitable for collecting much larger datasets, typically in 1–2 km wide swaths that can extend tens to hundreds of kilometers along linear targets such as fault traces, coastlines, or infrastructure corridors (e.g. Toth et al., 2007; Prentice et al., 2009; Hubbard et al., 2011; Oskin et al., 2012; Langridge et al., 2014; Clark et al., 2017; Johnson et al., 2018). ALS generally yields much lower point densities than TLS with typical values for modern acquisitions being 10–15 pts/m^2. Other limitations associated with ALS include the steep cost of deploying a crewed fixed-wing aircraft (10s to 100s of thousands of dollars per survey), restrictions on what altitudes and speeds they can fly at (which limits the raw point density), and constraints on scanning angles that can prevent penetration of the densest vegetation (VanValkenburgh et al., 2020; Resop et al., 2019). Rotary-wing aircraft (helicopters) are less constrained in terms of altitude and speed and have been used to achieve higher point density in some lidar surveys (Chen et al., 2015), but are generally even more cost-prohibitive.

Recently, a proliferation of inexpensive uncrewed aerial vehicles (UAVs)—commonly referred to as 'drones' and formally as remotely piloted aircraft systems (RPAS)—have provided a more accessible means of terrain mapping, including for seismology and active tectonics (e.g. Bemis et al., 2014; Johnson et al., 2014; DuRoss et al., 2019). Until very recently, this has involved deploying cameras and using sophisticated photogrammetric algorithms to create Digital Surface Models (DSMs) (e.g. Harwin and Lucieer, 2012; James and Robson, 2012; Westoby et al., 2012), with consequently only very limited ability to map forested landscapes. However, the recent development of smaller, lighter laser scanners has opened up the possibility of collecting lidar datasets from UAV platforms, referred to from now on as drone lidar or UAV laser scanning (ULS) (Wieser et al., 2016). This new advancement has seen some early adoption in the fields of archaeology (Risbøl and Gustavsen, 2018; VanValkenburgh et al., 2020), forestry and ecology (Brede et al., 2017; Kellner et al., 2019; Tomsett and Leyland, 2021), and fluvial and landslide geomorphology (Resop et al., 2019; Pellicani et al., 2019), but its effectiveness for mapping active faulting has not yet been demonstrated.

This paper introduces a state-of-the-art ULS system (Fig. 1) developed at the University of Victoria to study the geomorphology of putative active faults across the Canadian Cordillera. This is a region of widespread seismicity (Ristau et al., 2007) and elevated seismic hazard (Kolaj et al., 2020), but aside from the major plate boundary faults, only a few seismogenic faults have been conclusively identified and mapped owing to steep terrain, dense forest cover, and recent glaciation (e.g. Morell et al., 2017; Harrichhausen et al., 2023). We begin in Section 2 by describing the drone platform and instrumentation as well as our data collection, processing and analysis workflows. Our aim here is to provide a blueprint for other seismologists and geomorphologists interested in developing their ULS systems. In Sections 3–6, we then showcase examples of ULS lidar data collected using our drone platform along four faults with differing surface expressions in four unique types of vegetation cover from across western Canada (Fig. 2 and Table 2). The spatial scales of these case studies vary from a paleoseismic trench site with dimensions of a few hundred meters surveyed in a few hours (Harrichhausen et al., 2023) to regional acquisitions along fault sections totalling several kilometers in length mapped over several days (Finley et al., 2022a). In each case study, we compare the ULS data both quantitatively and qualitatively with existing ALS data, as well as SfM data where available. Particular focus will be on vegetation penetration performance, achievable ground return densities, and their impacts on derived DTM resolutions for the different lidar acquisition modes. In Section 7, we assess the impact of UAV flight speed on survey duration, point density and data quality, before discussing the unique applications, advantages, and limitations of ULS in active tectonics research. One of the principal advantages is simplified and cheaper repeat observations, with the potential for imaging co-seismic rupture, off-fault deformation, and post-seismic afterslip at finer spatial (<50 cm) and temporal (<1 day) resolutions. Additionally, the higher spatial resolutions attainable with ULS allow for more confident measurement and interpretation of subtle fault scarp morphology. The limitations of ULS systems include spatial coverage, which is restricted by battery life, flight constraints imposed by civil aviation authorities, and the

Term	Description
AGL	Above ground level.
ALS	Airborne laser scanning—lidar from a crewed aircraft. Synonymous with ALSM and airborne lidar.
ALSM	Airborne laser swath mapping—lidar from a crewed aircraft. Synonymous with ALS and airborne lidar.
BVLOS	Beyond visual line-of-sight.
DEM	Digital Elevation Model—a 3-D representation of terrain heights. Synonymous with DTM.
DoD	DEM of Difference—an elevation difference map between two DEMs.
DSM	Digital Surface Model—a 3-D representation of Earth surface heights, incl. natural or man-made objects.
DTM	Digital Terrain Model—a 3-D representation of terrain heights. Synonymous with DEM.
GCP	Ground control point—an identifiable point on Earth's surface with known location used for geo-referencing.
GNSS	Global Navigation Satellite Systems—a system that uses satellites to provide autonomous geopositioning.
GPS	Global Positioning Systems—the world's most utilized GNSS, and sometimes used synonymously.
ICP	Iterative closest point—an algorithm used to co-register two point clouds.
IMU	Inertial Measurement Unit—a device that tracks orientation using magnetometer, accelerometer, and gyro.
INS	Inertial Navigation System—a device integrating an IMU and GNSS.
.LAS	Industry standard binary file format used for the interchange and archiving of lidar data.
.LAZ	Compressed file format used for the interchange and archiving of lidar data.
lidar	Light detection and ranging, with varied capitalization (LiDAR, LIDAR, Lidar). Synonymous with laser scanning.
MLS	Mobile laser scanning—lidar from a roving scanner on or tethered to Earth's surface.
M3C2	Multiscale Model to Model Cloud Comparison— a method that measures differences between point clouds.
PPP	Precise Point Positioning—a GNSS method that calculates positions with errors of a few centimeters.
RINEX	Receiver Independent Exchange Format—a data interchange format for raw GNSS data.
RPAS	Remotely Piloted Aircraft System. Synonymous with UAV and drone.
RTH	Return to Home—a feature of some UAS that allows the drone to return autonomously to its take-off point.
sbet	Smoothed best estimate of trajectory—relating to the processing of UAV flight paths.
SfM	Structure-from-Motion—an algorithm for estimating 3-D scene structure from a set of photographs.
sUAS	Small Unmanned Aircraft System—a UAV weighing less than 25 kg.
TLS	Terrestrial Laser Scanning—lidar from one or more stationary locations on Earth's surface.
UAS	Uncrewed Aircraft System—a UAV and its accessories (e.g. ground control, transmission).
UAV	Uncrewed Aerial Vehicle. Synonymous with RPAS or drone.
ULS	UAV Laser Scanning—lidar from a UAV platform, also referred to here as "drone lidar".
VLOS	Visual line-of-sight.

Table 1 Acronyms and initialisms used in this paper and/or common within the wider literature on drone-based and lidar remote sensing, with abbreviated definitions where helpful.

Section	Fault	Target and landscape description	Vegetation Type	Area (km^2)	Time to Collect
3	X̱EOLX̱ELEꝀ - Elk Lake fault, Vancouver Island	Reverse fault scarp within a suburban park	Pacific Dry Forest	0.01	5 hours (1 day)
4	San Juan fault, Cowichan Valley, Vancouver Island	Strike-slip fault within a steep-sided valley	Pacific Cool Temperate Forest	2.8	14 hours (2 days)
5	Southern Rocky Mountain Trench fault, East Kootenay	Suspected fault scarp crossing gently-sloping alluvial fans	Cordilleran Dry Forest	3.1	16 hours (3 days)
6	Eastern Denali fault, Kluane Lake	Major strike-slip fault in a broad glacial valley	Northwestern Boreal forest	10.4	12 days

Table 2 Summary of case studies described in this paper. The drone lidar platform was tested in several different tectonic settings and climatic regions along faults of a variety of kinematic styles within the Canadian Cordillera in British Columbia and the Yukon. Canadian vegetation types are from Baldwin et al. (2019).

necessity of road access to launch sites with good visual sightlines, and we finish the paper by discussing ways in which these limitations might be mitigated in the future.

2 Methods

2.1 The ULS system

Our ULS platform was built using several commercially available and custom-built components (Fig. 1). The former comprise a DJI Matrice 600 Pro hexacopter, a Riegl miniVUX-1UAV laser scanner, an Applanix APX-20 UAV Inertial Navigation System (INS), and a Trimble AV14 antenna. Custom-built elements include an interface board used to integrate the laser scanner and INS and a housing and mounting mechanism. The 2.75 kg payload is mounted to the drone with a dovetail-style connector, similar to those used in motion-stabilized gimbals for cinematography.

The DJI Matrice 600 Pro hexacopter has a payload capacity of 6 kg, more than double what we deploy. It uses one set of six TB47S Lithium-Ion Polymer batteries per

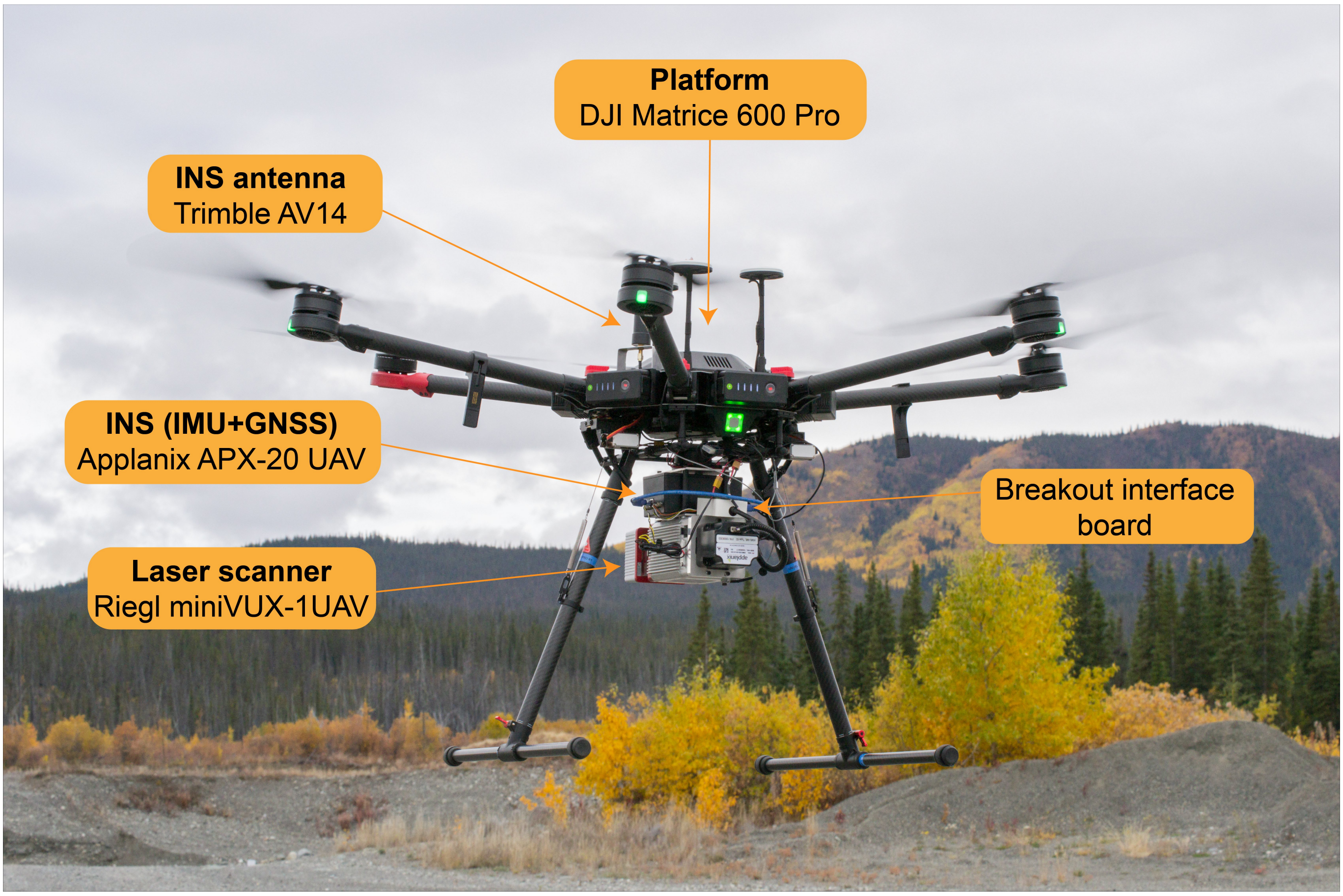

Figure 1 Annotated photograph of the drone platform and instrumentation used in this study. For scale, the full diameter of the drone, including rotor blades, is 1.66 m.

flight (4500 mAh), enough power for ~20 minutes of flying with our payload. Notably, these batteries are just below the 100 watt-hour rating restriction imposed by civil aviation authorities, allowing us to travel to field sites with the drone system via commercial airline. The drone is maneuvered via a remote controller and transmitter with a manufacturer-stated maximum operating distance of 5 km, though in practice, we begin to encounter connectivity issues beyond ~1.5 km in forested and mountainous terrain. The pilot must abide by flight constraints imposed by civil aviation authorities, including altitude limits of 400 ft (121.92 m) above ground level (AGL) in both Canada and the U.S., restrictions to flights over people, and maintenance of visual line-of-sight between the pilot (or a visual observer in constant radio contact with the pilot) and the drone. Many countries have similar UAV regulations, although exact parameters for flight height and horizontal distance do vary (Stöcker et al., 2017). In Canada, pilots must have obtained Advanced Operations drone pilot certification from Transport Canada (Transport Canada, 2022) through an online multiple-choice test and an in-person flight review. This certification allows the pilot to operate in controlled airspace with any drone weighing less than 25 kg. Many other national aviation authorities offer similar certifications (e.g. Federal Aviation Administration, 2023; UK Civil Aviation Authority, 2023; European Union Aviation Safety Authority, 2022; Civil Aviation Safety Authority, 2021).

Weighing 2 kg and with a manufacturer-stated optimum altitude of 80 m AGL, the miniVUX-1UAV laser scanner is specifically designed for deployment from a drone. It offers an eye-safe laser (at Laser Class 1) with a pulse repetition rate of 100 kHz and a 360° field of view. The laser footprint diameter at optimum altitude is 6.4 cm at nadir and 9 cm at 45° from nadir. The scanner can record up to 5 returns from a single laser pulse, making it suitable for application in densely vegetated areas where SfM terrain mapping would be unfeasible. The Applanix APX-20 UAV INS integrates a Global Navigation Satellite Systems (GNSS) device and an Inertial Measurement Unit (IMU), which together with the attached Trimble AV14 antenna track the precise location and orientation of the laser scanner. This allows the coordinates of points within the final point cloud to have sub-decimetric accuracies (3–5 cm). The breakout board interfaces with the laser scanner using a customized circuit board which allows communication and timing between components, streams data between the INS and the laser scanner, and distributes power to both of these systems.

Our ULS system also makes use of a range of auxiliary equipment (Figure 3A). This includes a Trimble R12 GNSS base station (and tripod) for post-processing the drone trajectory and—if the best possible absolute georeferencing is desired—a separate Trimble R12 GNSS rover unit, TSC7 handheld computer and monopod for surveying ground control points (GCPs). For these we

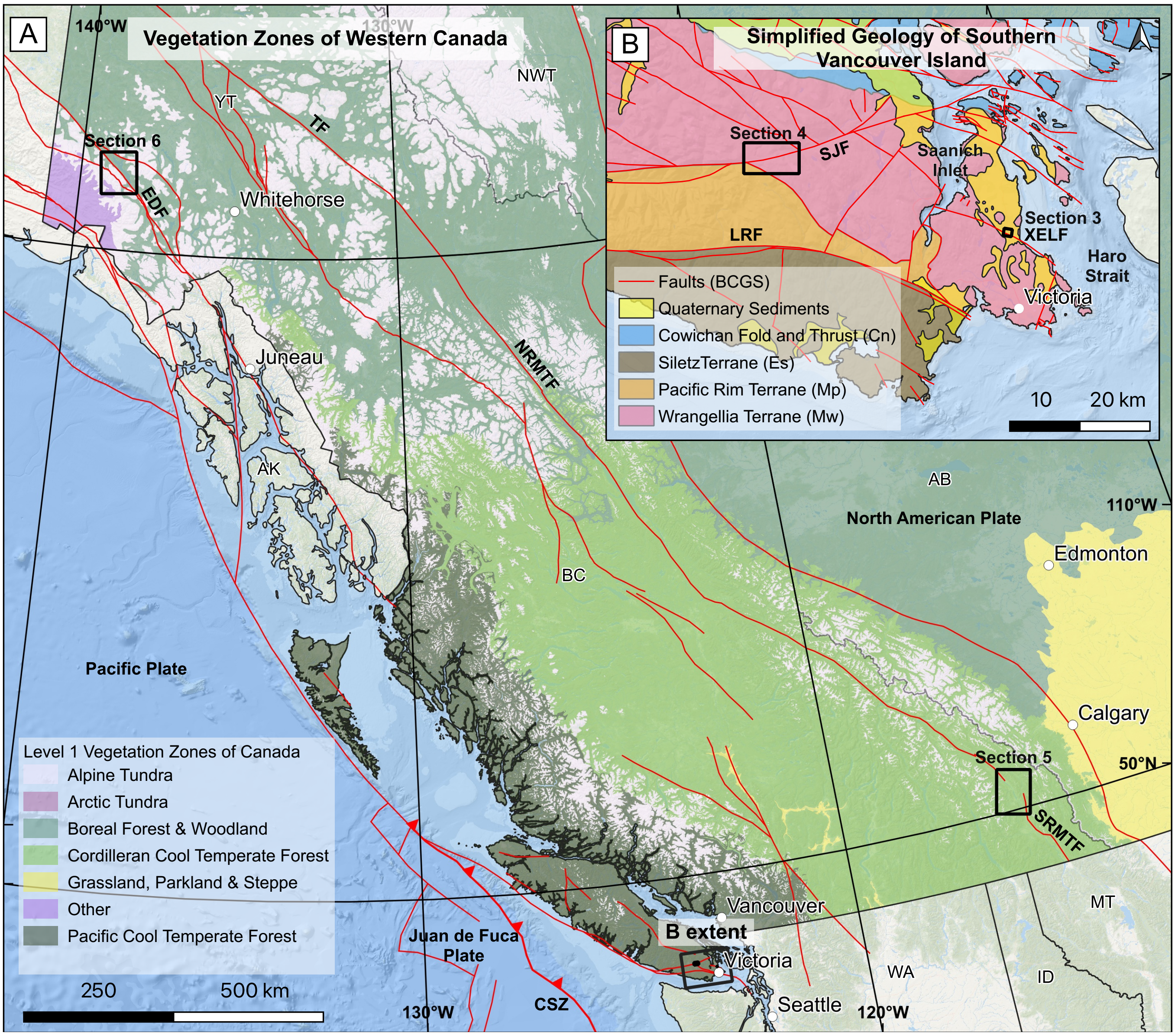

Figure 2 Location of case study sites (Table 2). (A) Level 1 Vegetation zones for Canada from Baldwin et al. (2019). Major faults are in red, some of which have been labelled. CSZ: Cascadia Subduction Zone, EDF: Eastern Denali fault, NRMTF: Northern Rocky Mountain Trench fault, SRMTF: Southern Rocky Mountain Trench fault, TF: Tintina fault. (B) Simplified geological map for southern Vancouver Island with major faults labelled, modified from the BC Geological Survey compilation by Cui et al. (2017). LRF: Leech River fault, SJF: San Juan fault, XELF: X̱EOLX̱ELEꝀ-Elk Lake fault. Abbreviations for states, provinces and territories are as follows; AB: Alberta, AK: Alaska, BC: British Columbia, ID: Idaho, MT: Montana, NWT: Northwest Territories, WA: Washington, YT: Yukon. Background imagery is from Esri (2022).

use 120 cm × 120 cm fabric harlequin-iron cross targets, which we secure to the ground with hammer and nails. We also pack a field laptop with flight planning software installed, an iPad or cell phone to connect to the radio controller, walkie-talkies to allow constant communication between crew members, an inverter generator (minimum 2200 watts to support all charging needs), charging equipment and spare drone batteries to allow a quick succession of repeat flights, and field safety gear. All of the equipment fits inside our Jeep Wrangler field vehicle with room for three crew members and their personal gear.

2.2 Survey planning

Initial planning starts with consideration of three factors. Firstly, as our drone platform and auxiliary equipment (Figure 3) are too bulky to be carried easily by foot, launch sites must be accessible via vehicle. Existing coarse resolution DTMs, satellite imagery, and Google Streetview are great tools for identifying such spots. In areas with steep topography or forest cover, visual-line-of-sight is often impossible to maintain from the launch site and so we use one or more visual observers positioned in areas with good sight lines in constant communication with the drone pilot via walkie-talkie. Secondly, if the survey is located within classified airspace, approval must be applied for in advance. In Canada this can be done online through NAV Canada's NAV drone application. Thirdly, in the days leading up to the fieldwork we check the weather forecasts, as our drone cannot operate in any form of precipitation or in winds that are greater than 8 m s^{-1}.

Once these initial considerations are addressed, we use drone flight planning software to generate automated flight paths for our data collection. Map Pilot Pro by Maps Made Easy and Universal Ground Control Station (UgCS) by SPH Engineering have both been used successfully for this purpose, with the latter our current preference since it allows more control over survey design (custom base maps and images), flight parameters (e.g., altitude, speed), and laser parameters (e.g., field of view, swath overlap) such that a desired point density is achieved. There is a trade off between point density and areal coverage and the specific scientific goals of the survey need to be considered. These parameters are fine-tuned using Riegl's RiParameter software to ensure even point spacing, and set in the laser instrument using the RiAcquire tool. We discuss optimization of these parameters in section 7.1. Typical flight plans for fault-related studies consist of 2–8 strike parallel survey lines, and 2 cross-track lines for the purposes of track alignment in post-processing (Figure 3B). For larger surveys these will be undertaken in multiple flights in order to allow for battery replacement. Note that each individual flight must have a minimum of two overlapping lines, and it is best practice to design surveys that allow for the completion of full lines, rather than abandoning and resuming part-way along a line; overlapping data is critical for scanline alignment when merging flights in post-processing. In fault surveys when the desire is to achieve maximum coverage along-strike, the most efficient flight plans in our experience consume ∼35% battery on the outward track and ∼35% on the return track, allowing the drone to return to home safely at 30% battery, the depletion threshold recommended by the manufacturers. Survey extents are further limited by the need to maintain visual line-of-sight between the pilot, or one or more visual observers in constant radio contact with the pilot, and the drone. In the absence of obstacles we find this visual limit to be around ∼1.5 km, though it is often challenging in forested areas to find ideal sight lines. In practice, considering battery, radio controller connectivity, and line-of-sight requirements, we find that survey lengths from an individual launch site are limited to a maximum of ∼1.8 km even with visual observers present. Flight paths for the case studies presented in this study are provided in the supplemental material (SM1–11) to illustrate survey patterns required for different spatial extents and terrain.

2.3 Data acquisition

On the day of the survey, we drive to our launch site where we first set up the GNSS base station (Figure 3C). Getting the base recording started early ensures that there is a sufficiently long (minimum 3 hour) base observation for post processing the flight trajectories. The drone platform is assembled and the laser and IMU payload mounted onto it. Before uploading the automated flight plan, a short, manual test flight ensures that the controller is operating as expected and that the drone's gyroscope and magnetometer are calibrated. If desired, GCPs can be placed in 4–6 locations scattered across the survey footprint and clear of forest cover. These locations should ideally be situated beneath multiple overlapping and orthogonal flight lines. It is expedient to deploy GCPs before or during the drone setup and test flight, often by our visual observers as they move into position. In order to calibrate the IMU, the drone system is powered up and sits for 5 minutes of static calibration, followed by a dynamic calibration that involves accelerating, decelerating and strafing to the left and right. Finally, the flight plan is uploaded to the drone from our field laptop or tablet, after making any last minute adjustments as needed. The entire set-up period, from arriving at the launch site to the start of the first survey flights, typically takes an hour with two or three people present.

The drone is then launched and its automated flight pattern started, with pilot and visual observers in constant radio communication to ensure that it is always within sight and maintaining sufficient clearance of obstacles. Once the batteries approach the 30% depletion threshold, the drone is brought back to the landing spot, and the static calibration is repeated before the system can be powered down and the batteries changed for fresh ones. For larger surveys, it is necessary to bring several sets of batteries and generator to recharge depleted batteries and keep flying throughout the day. At our highest levels of operating efficiency, we find that 6 sets of 6 batteries (TB47S) and two DJI Hex Chargers, running simultaneously and continuously, are necessary to keep pace with surveying. Once the full survey has been successfully flown, the base station needs to remain running for a minimum of half an hour to ensure that its location is well constrained, as is recommended in both Riegl and Applanix documentation. If we are surveying GCPs with a GNSS rover, we usually do this after the final drone flight, and leave the base station running yet another half an hour as we pack up the remaining gear.

2.4 Data Processing

After a successful survey, data from the laser scanner, the INS, and the GNSS base station and rover are copied to a workstation for processing. We follow the workflow summarized in Figure 4, which includes several pre-processing steps before the final point cloud is generated. The first step involves processing the GNSS data collected by the base station and rover. The base observation file is converted to RINEX format and uploaded to Natural Resource Canada's (NRCan) Precise Point Positioning (PPP) tool to post-process the GNSS observations and calculate an accurate base position using satellite orbit, clock and bias corrections. GCP locations surveyed with the rover can then be adjusted using the corrections to the base location from the PPP processing. The revised GCP locations are uploaded to the NRCan GPS-H tool to convert their ellipsoidal heights into orthometric heights, and the final coordinates exported as a csv file. The NRCan tools are free

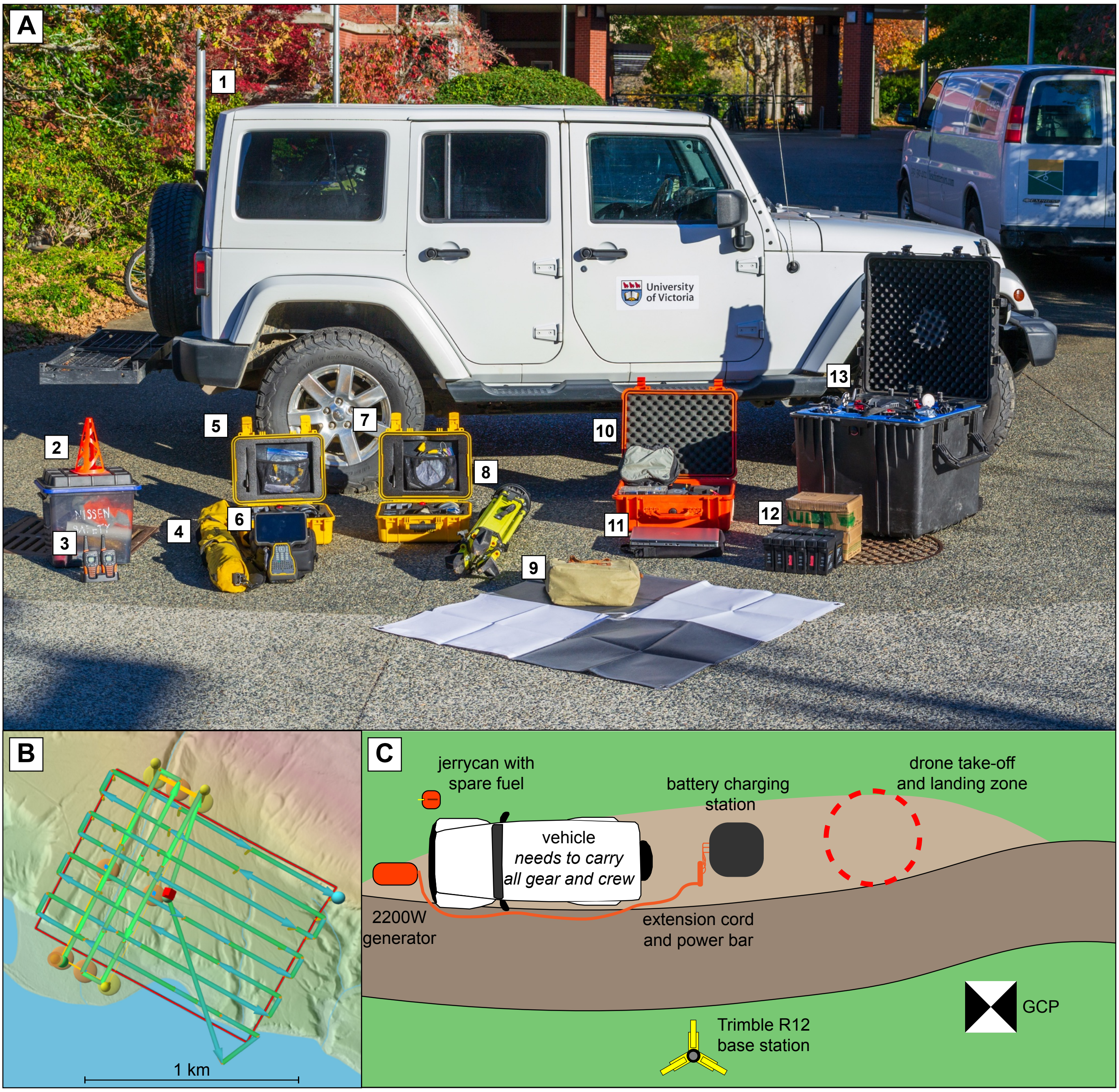

Figure 3 (A) Equipment needed for a typical acquisition. (1) Four-wheel drive vehicle. (2) Safety gear including first aid kit, traffic cones, high-visibility vests, and fire extinguisher. (3) Walkie-talkie radios for pilot and visual observers, plus chargers. (4) Trimble monopod for GNSS rover. (5) Trimble R12 GNSS rover in Pelican case. (6) TSC7 handheld computer for Trimble system. (7) Trimble R12 GNSS base station in Pelican case. (8) Trimble tripod for GNSS base station. (9) GCP targets, hammer and nails in carry bag. (10) Riegl miniVUX-1UAV laser scanner, Applanix APX-20 UAV INS, and assembly toolkit in Pelican case. (11) Windows laptop with UgCS flight planning and Riegl lidar processing software installed. (12) At least four but preferably six sets of batteries for the drone, plus two DJI Hex Chargers. (13) DJI Matrice 600 Professional hexa-copter in its customized carry-case (dimensions 68 cm × 53 cm × 49 cm). Not pictured: field iPad (to connect to the radio controller), generator (minimum 2200 W), extension cord, powerbar, and tarpaulin. (B) Flight line planning in UgCS for a segment of the Southern Rocky Mountain Trench acquisition (Section 5). The red pin is our launch site, the red box is our specified target area, and the blue-green lines are the drone flight lines. (C) Sketch-map showing a typical roadside survey set-up.

for use within the Canadian landmass, but other free online PPP options are available for use outside of Canada including; the National Geodetic Survey's Online Positioning User Service (OPUS, https://geodesy.noaa.gov/OPUS/index.jsp), GNSS Analysis and Positioning Software (GAPS) (Leandro et al., 2011), magicGNSS (Piriz et al., 2008), and the Automatic Precise Positioning Service (APPS) which uses JPL's GipsyX/RTGx software (Bertiger et al., 2020). The next pre-processing step involves refining the drone trajectory using INS data from the Applanix APX-20 UAV and converting this to orthometric heights. Working in Applanix's POSPac UAV software, the INS data are imported into a project and the base station observation added. The inertial processing tool is run to produce a smoothed best estimate of the trajectory (sbet), which is then exported in orthometric heights for import into the proprietary laser processing software (RiWorld).

We process the MiniVUX-1UAV lidar data in Riegl's proprietary RiProcess software. Each flight produces an individual laser file and associated trajectory. These are imported into the laser project and used to create an initial point cloud. The trajectories can be edited to remove unwanted data collected during turns or transits of the drone, leaving only data collected along the main survey lines. This is an important step as accelerations, decelerations, and rotations during turns and transits can negatively impact the final point cloud, creating sections with an uneven spacing of points. Once the point cloud has been sufficiently cleaned in this way, the individual flights can be merged into a single project. GCP coordinates can then be added by importing the csv file from GPS-H processing, and used to adjust and align the point clouds. In order to select the corresponding points in the laser file, we find that the cloud is best visualized using the reflectivity option. We select several points nearest the center of each GCP target and average their elevations to account for centimetric vertical scatter. Once target centerpoints have been added for several flight lines, the flight line point clouds can be precisely georeferenced, aligned, and adjusted using the RiPrecision tool. Flat hard surfaces can be used to check the amount of scatter present within the point cloud. Many of our field sites are in remote regions with limited options for additional, independent ground control, and we have therefore not performed testing of georeferencing uncertainties of our system against geodetic control monuments. However, we estimate uncertainties in the order of ∼20 cm, based on random scatter observed in our point clouds (∼15 cm) as well as expected accuracies of our GNSS ground control. We acknowledge that constraining these errors is important, especially for applications involving change detection between multiple acquisitions. However, our ∼20 cm estimate compares favourably with uncertainties associated with ALS datasets, such as errors of ∼21 cm observed by Hodgson and Bresnahan (2004) over a range of land cover types, and horizontal and vertical errors of ∼29 cm and ∼9 cm observed by Glennie et al. (2013) in helicopter lidar acquisitions.

Once the flight lines have been aligned and georeferenced, an unclassified point cloud can be exported for final classification, cleaning and gridding, for which we use a variety of programs within the licensed LAStools package (Isenburg, 2021). A copy of the shell script for classifying and rasterizing the raw lidar point cloud can be found in the supplemental material (SM12). To determine ground points we use lasground_new, a progressive morphological filter (Zhang et al., 2003). There are alternate options for ground classification, such as simple morphological filtering (Pingel et al., 2013) or cloth simulation filtering (Zhang et al., 2016), both of which can be freely used with the Point Data Abstraction Library (PDAL), an open-source library for processing and analysing point clouds (Butler et al., 2021). However, we prefer lasground_new because it has several parameters such as step, spike and bulge that can be adjusted to best find ground points according to the environment in which the data were collected, and which works well on steep, forested slopes (Căţeanu et al., 2017) that are prevalent in western Canada. Once the ground returns have been determined, we classify the remaining points using lasclassify. Other, optional steps at this stage of processing include tiling the point cloud to allow for efficient multi-threaded processing and clipping it to a polygon of interest. Isolated noise points within the cloud are then removed using lasnoise before a DTM can be generated by rasterizing the ground points with lasgrid. Lasgrid can also be used to export other desired parameters such as point density per pixel, intensity, scan angle, and (if available) RGB values. The same LAStools parameters were used to process each dataset, with the only differences being the cell size for the resultant raster products, listed in Table 3.

2.5 Data comparisons and differencing

In Sections 3–6, we compare our fully processed drone lidar data with overlapping airborne lidar and SfM surveys in order to assess their consistency and to determine from any differences whether drone lidar offers advantages over the more established methods. For these analyses, we first used the iterative closest point (ICP) algorithm available within free CloudCompare software (http://www.danielgm.net/cc/) to perform a final registration of the drone and comparison point clouds. The ICP algorithm finds a rigid body transformation (translation and rotation) that iteratively minimizes the closest point pair distances between two point clouds. This step was taken in order to account for several sources of error, including random scatter within each point cloud, potential differences in the global registration of the two datasets including use of different vertical datums, and/or uncertainties within the control used to georeference either dataset. Consequently, remaining differences between the datasets (see below) will largely represent differences in the way each method characterizes the ground surface, coupled with (likely minor or localized) natural or anthropogenic landscape change that may occurred between each pair of surveys.

We used CloudCompare's M3C2 (Multiscale Model to Model Cloud Comparison) plugin (Lague et al., 2013) to calculate the distance between ground points within the compared datasets. The M3C2 algorithm computes the local distance between two point clouds along a normal surface direction. This calculation is performed upon the point clouds, without any meshing or gridding, providing a signed 3-D distance as opposed to alternative techniques which only offer either 2-D differences (e.g. vertical difference maps) or unsigned 3-D differences (CloudCompare's cloud-to-cloud distance tool). Additionally, the M3C2 method is designed for application to datasets of contrasting point spacings (Lague et al., 2013; DiFrancesco et al., 2020), and is thus well-suited for comparing dense drone lidar datasets with coarser airborne datasets. Within CloudCompare, the drone

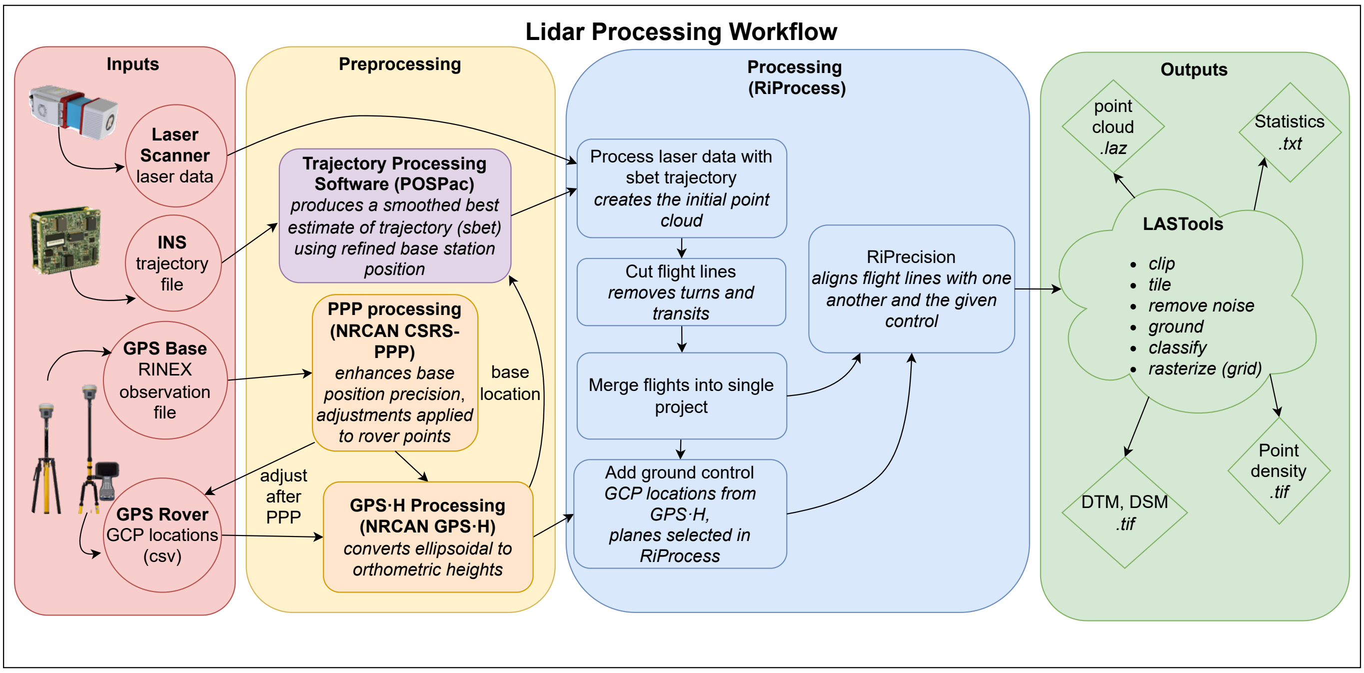

Figure 4 Flow diagram summarizing our ULS data processing workflow. Abbreviations used in this figure; DSM: Digital Surface Model, DTM: Digital Terrain Model, GPS: Global Positioning Systems, INS: Inertial Navigational System, NRCAN: Natural Resources Canada, PPP: Precise Point Positioning, sbet: smoothed best estimate of trajectory.

lidar dataset was selected to be cloud #1 and the airborne lidar or SfM dataset as cloud #2. The sign of the distance reflects where the reference point cloud was along the direction of the normal for each core point. For example, a negative M3C2 value indicates an area where the drone lidar data are located underneath the airborne lidar. The cloud distances were calculated with the 'multi-scale' option, meaning that the normal distances could be in any combination of horizontal and vertical. The coarser of the two datasets was used to determine the core points as its wider point spacing reduces the number of computations required. The plugin produces a point cloud containing the M3C2 distances and areas with significant change as additional attributes. This was saved and rasterized, highlighting internal differences between the point clouds.

We further quantified disparities in the raster models produced for the drone lidar and comparison datasets by calculating their DEMs of Difference (DoD). For this, the drone lidar was first re-gridded (post point cloud alignment) at the same resolution as the airborne lidar DTM or SfM DSM, before the vertical topographic differencing was performed using the Geospatial Data Abstraction Library's gdal_warp tool (GDAL/OGR contributors, 2023). Following the methodology and conventions of Scott et al. (2021), the compare dataset (the newer drone lidar DTM) was subtracted from the reference dataset (the older airborne lidar DTM or SfM DSM). As such, negative DoD values represent areas in which the drone lidar DTM is lower than the reference ALS or SfM model, and vice versa. Note that this distance is purely vertical, unlike the M3C2 distances which are normal to the sparser of the point clouds. A shell script for differencing DTMs and generating histograms is provided in supplemental material (SM13).

3 The X̱EOLX̱ELEꝀ-Elk Lake fault: a local survey of a paleoseismic trench site

3.1 Background and motivations

The X̱EOLX̱ELEꝀ-Elk Lake fault (XELF) is a newly-recognized active crustal fault within the fore-arc of the northern Cascadia subduction zone on southern Vancouver Island, BC (Harrichhausen et al., 2023). The fault is named after X̱EOLX̱ELEꝀ (pronounced *hul-lakl-lik*), the name given to Elk Lake by the W̱SÁNEĆ people. The XELF was first identified from provincial airborne lidar imagery (LidarBC, 2023) crossing Saanich peninsula between Saanich Inlet in the NW and Haro Strait in the SE (Figure 2B). The lidar data revealed several ∼N-facing fault lineaments including a 1-2.5 m high scarp displacing the surface of a Pleistocene glacial landform—a large, N–S drumlinoid ridge—between X̱EOLX̱ELEꝀ (Elk Lake) and Haro Strait. A site was chosen for paleoseismic trenching between the eastern lake shoreline and the Patricia Bay Highway, where the scarp passes through Elk-Beaver Lake Regional Park. The trench, excavated in August 2021, contained evidence that indicated the XELF has ruptured in at least one large (M_w ∼6.1–7.6) thrust earthquake during the late Holocene (Harrichhausen et al., 2023).

The eastern X̱EOLX̱ELEꝀ (Elk Lake) shoreline site (Fig. 5A–B) provided an early and relatively simple test of our new ULS system, acquired prior to the planned trench and providing the best possible data for measuring the local scarp height. The survey area has dimensions of just ∼100 m and exhibits gentle relief other than a steep bank up to the Patricia Bay Highway along the eastern boundary. The ground cover is mostly mowed grass as well as scattered blackberry bushes, decidu-

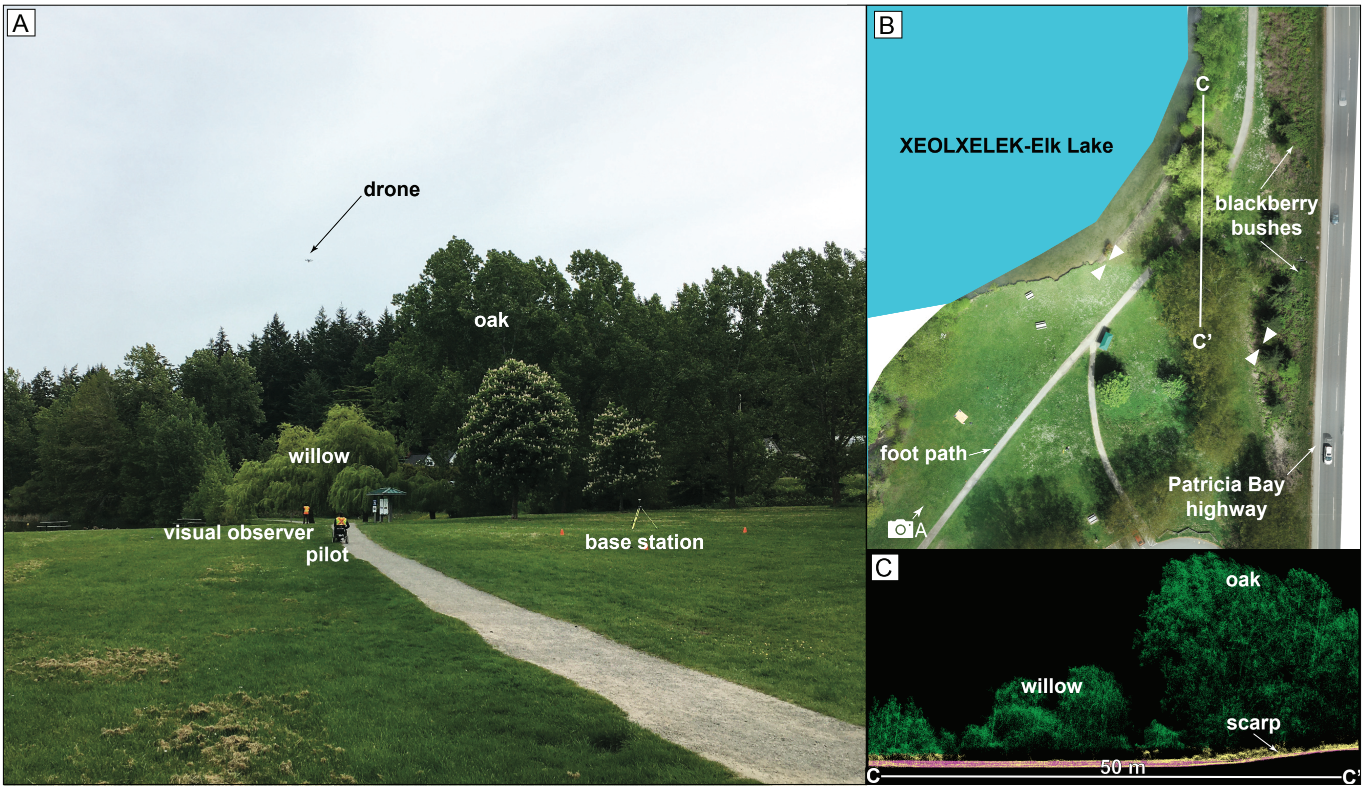

Figure 5 (A) Field photo showing ULS data collection at the eastern X̲EOLX̲ELEꝀ (Elk Lake) shoreline site. The photo location and orientation are shown in (B). The visual observer stands at the top of the XELF scarp and at the approximate mid-point of the future, NE-trending paleoseismic trench (Harrichhausen et al., 2023). (B) SfM-derived orthophoto of the acquisition site. White triangles indicate the location of the fault scarp. (C) Cross section C—C' through part of the classified drone lidar point cloud. Green points are vegetation, pink are ground points, and yellow points are unclassified.

ous trees (willow and oak) and conifers (Douglas Fir and Western Red Cedar), the tallest of which are around 35 m. Since the site lies within the municipal Elk-Beaver Lake Regional Park and on traditional W̲SÁNEĆ territory, further permissions had to be obtained to conduct research and operate a drone within the park, in addition to the civil aviation approvals described in Section 2.2 (see Acknowledgments).

3.2 ULS data acquisition and results

We surveyed the eastern X̲EOLX̲ELEꝀ (Elk Lake) shoreline site with our drone lidar system in May 2021 (Fig. 5A), three months prior to the paleoseismic trench excavation by Harrichhausen et al. (2023). Our 100 m × 110 m ($\sim$11,000 m^2) drone lidar dataset took a total of 4 hours to collect, including set-up, with a crew of a pilot, two visual observers, and two assistants who helped avoid flying over pedestrians in the busy park (see Section 2.1). The drone was flown at a height of 45 m AGL in a cross-hatch pattern of N-S and E-W flight lines (supplementary Figure SM1) and at a relatively slow speed of 2 m s^{-1}. These parameters were chosen in order to collect as high a resolution dataset as possible, with an expectation of >100 pts/m^2. At 45 m AGL the laser footprint is 3.6 cm at the center of each 90 m-wide swath and 5 cm at the edges of the swath. Three GCPs were deployed and used to georeference the dataset.

Processing and classifying the drone lidar data using the workflow described in Section 2.4 yielded an average point density of 543 pts/m^2 and an average classified ground return density of 260 pts/m^2, leading to an average ground return spacing of $\sim$6 cm (Figure 6A–B, middle column, and Table 3). Classified ground returns constitute $\sim$48% of all points in the cloud. As expected, ground returns are densest away from the trees over areas of open, mowed grass, reaching values as high as $\sim$700 pts/m^2 where swaths from several flight paths overlap. However, a visual inspection of the classified point cloud in cross section also reveals successful imaging of the ground surface through tree and shrub foliage (Fig. 5C). We find that a cell size of 20 cm optimizes the ULS raster DTM, minimizing its pixel dimensions without introducing widespread data gaps (Fig. 6C, middle column). The cross-hatched point density pattern (Fig. 6B, middle column) results from the perpendicular orientations of the survey flight lines.

3.3 Comparisons and differencing with ALS and SfM data

Our first comparison dataset is the provincial airborne lidar survey, flown in 2019 and available from the LidarBC (2023) portal. Within the ULS survey footprint, the ALS point cloud yields an average point density of 14 pts/m^2, an average ground return density of 9 pts/m^2 for a spacing of $\sim$33 cm, and a maximum ground return density of 10 pts/m^2 (Figure 6A–B, left column, and Table 3). The ALS point cloud also contains more, and larger, data gaps than the ULS cloud, indicating greater

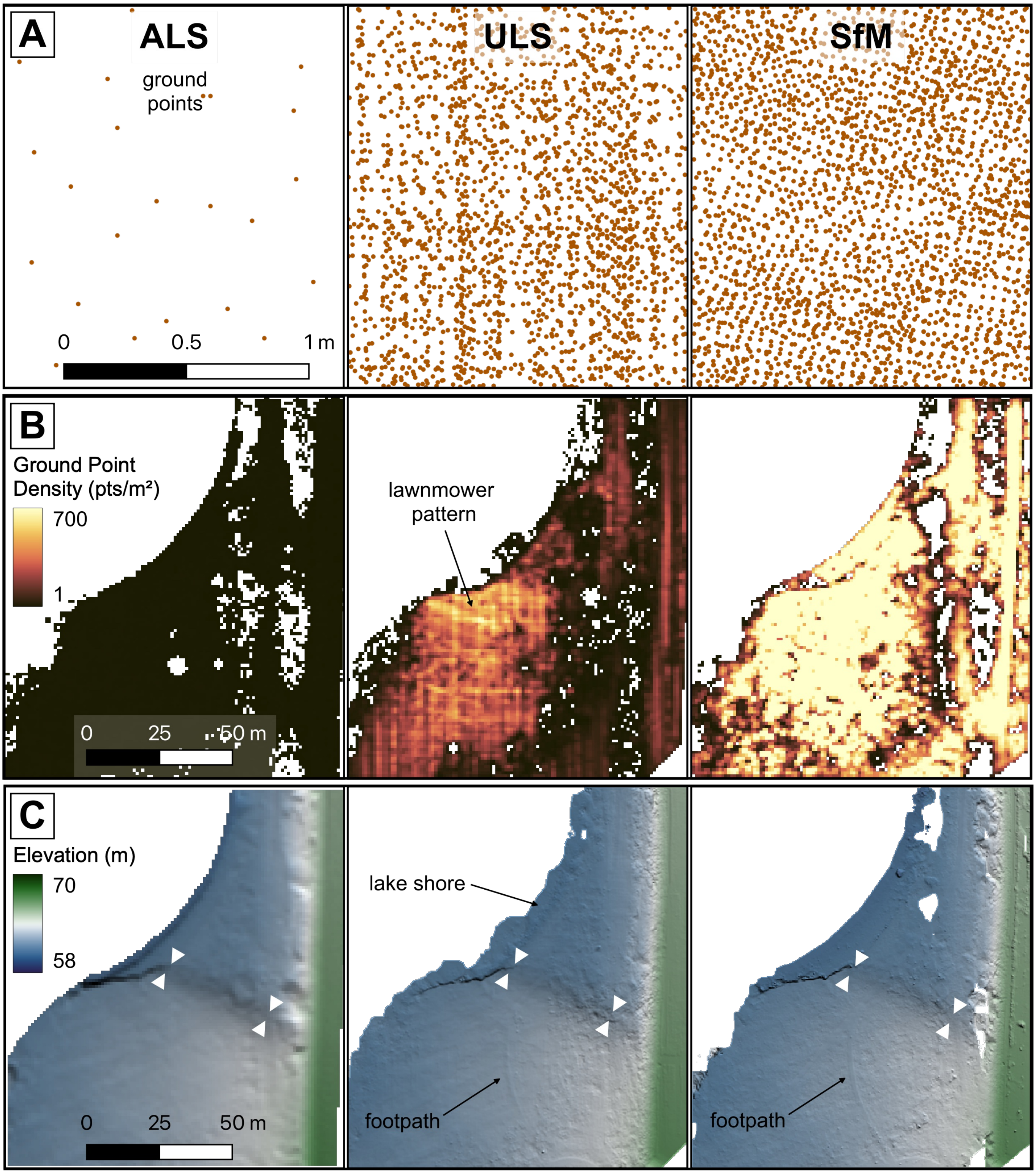

Figure 6 Comparison of topographic datasets at the eastern X̲EOLX̲ELEꝄ (Elk Lake) shoreline site: (left column) LidarBC ALS data, (middle) our ULS data, and (right) our SfM data. (A) Representative ground point clouds viewed at a roughly metric scale in order to contrast point spacings. (B) Survey-wide classified ground point densities. The same color palette is used for each plot, and white spaces indicate areas without ground coverage (mostly trees and dense blackberry bushes). (C) Hillshaded DTMs illuminated from the SSW (210°) in order to highlight the NNE-facing fault scarp, further delineated by white arrows. The DTMs were constructed with an interpolation of 5 pixels in order to minimize holes.

difficulty in imaging beneath vegetation. The ALS DTM has a cell resolution of 1 m, 25 times coarser than our ULS DTM (Figure 6C, left column). The fault scarp can be made out in both raster datasets as a gentle NNE-facing slope trending WNW-ESE across the center of the target area, but the finer resolvability of the ULS dataset is evident in a small linear depression along one of the park footpaths, which is not visible in the ALS DTM. Though not a tectonic feature, this does highlight the potential for ULS to identify subtler fault offsets than are

General Acquisition Information

Paper section	Fault (site)	Data type	Provider	Area (km^2)	Point density (pts/m^2)	Ground return density (pts/m^2)	Ground return spacing (m)	% pts ground	DTM cell size (m)
3.2	XELF	ULS	This study	0.01	543.39	260.11	0.06	48	0.2
	XELF	ALS	LidarBC		13.97	9.00	0.33	64	1.0
	XELF	SfM	This study		1906.16	554.04	0.04	29	0.2
4.2	SJF	ULS	This study	2.81	130.28	13.38	0.29	10	
	east			1.21	141.70	10.80	0.30	7	0.5
	west			1.59	121.59	17.24	0.24	13	0.5
	SJF	ALS	Mosaic		*(ground only)*	5.70	0.43	-	1.0
5.2	SRMT	ULS	This study	3.14	101.57	35.62	0.17	35	0.3
	SRMT	ALS	LidarBC		17.71	7.00	0.38	41	1.0
6.2	EDF	ULS	This study	10.42	97.54	45.47	0.21	47	
	BURW			0.37	92.75	25.95	0.20	28	0.3
	COPJ			1.02	79.60	25.46	0.20	32	0.3
	DUKE			4.86	112.33	71.78	0.19	64	0.3
	NINE			0.82	90.33	21.43	0.22	24	0.3
	QUIL			1.34	96.96	21.45	0.22	22	0.3
	SLIM			0.52	82.25	29.00	0.29	35	0.3
	TELL			1.49	81.61	19.69	0.23	24	0.3
	EDF	ALS	This study		7.85	3.45	0.54	44	1.0

			ICP transformation		**Differencing**			
Paper section	Fault (site)	Data comparison	Max rotation (°)	Translation vector (m)	M3C2		DoD	
					Mean (m)	SD (m)	Mean (m)	SD (m)
3.3	XELF	ULS–ALS	0.0008	0.28	−0.05	0.19	−0.32	0.26
	XELF	ULS–SfM	0.0005	0.33	−0.03	0.14	−0.27	0.27
4.3	SJF (east)	ULS–ALS	0.0001	0.07	0.22	0.42	0.21	0.62
	SJF (west)	ULS–ALS	0.0002	0.32	0.13	0.31	0.15	0.53
5.3	SRMT	ULS–ALS	0.0001	0.54	−0.01	0.09	−0.02	0.29
6.3	EDF (BURW)	ULS–ALS	0.0004	0.82	−0.01	0.14	0.01	0.26
	EDF (COPJ)	ULS–ALS	0.0002	0.87	−0.01	0.17	0.00	0.25
	EDF (DUKE)	ULS–ALS	0.0003	0.54	0.00	0.18	0.00	0.28
	EDF (NINE)	ULS–ALS	0.0002	0.99	0.01	0.18	0.01	0.23

Table 3 Statistics of our ULS and comparison datasets (upper part of the table) and of the ICP alignments and subsequent M3C2 and DoD differencing (lower part of the table). ALS statistics are calculated from within the footprints of the corresponding ULS surveys, allowing a like-for-like comparison. % pts ground is the percentage of all lidar returns classified as ground.

evident in traditional airborne lidar data.

Because much of the eastern X̱EOLX̱ELEꝀ (Elk Lake) shoreline site is covered by mowed grass, it provides our best opportunity out of all of our case studies to compare our drone lidar with SfM data. With this in mind, we surveyed the site with SfM two weeks before our drone lidar flights. Using a DJI Phantom 4 Professional V2 drone with the built-in camera, we captured 749 photographs which were then processed using the Agisoft Metashape Professional software package, with 15 GCPs deployed across the scene for georeferencing (e.g. Johnson et al., 2014). After classifying the SfM point cloud with the LAStools LASclassify program, we yielded an average point density of 1,906 pts/m^2 and average classified ground point density of 554 pts/m^2 and spacing of 0.04 m (Figure 6A–B, right column, and Table 3). However, the SfM is strikingly less uniform than either lidar point clouds, containing far more, and larger, data gaps, reflecting its inability to image beneath vegetation (Figure 6B). As a consequence, we find that the optimal resolution of the SfM DTM is 20 cm (Figure 6C, right column), no finer than the ULS DTM despite their differing underlying ground point densities.

The ICP rigid body transformation that most closely aligns the ULS point cloud to the ALS point cloud involved a translation vector of 28 cm and rotations of

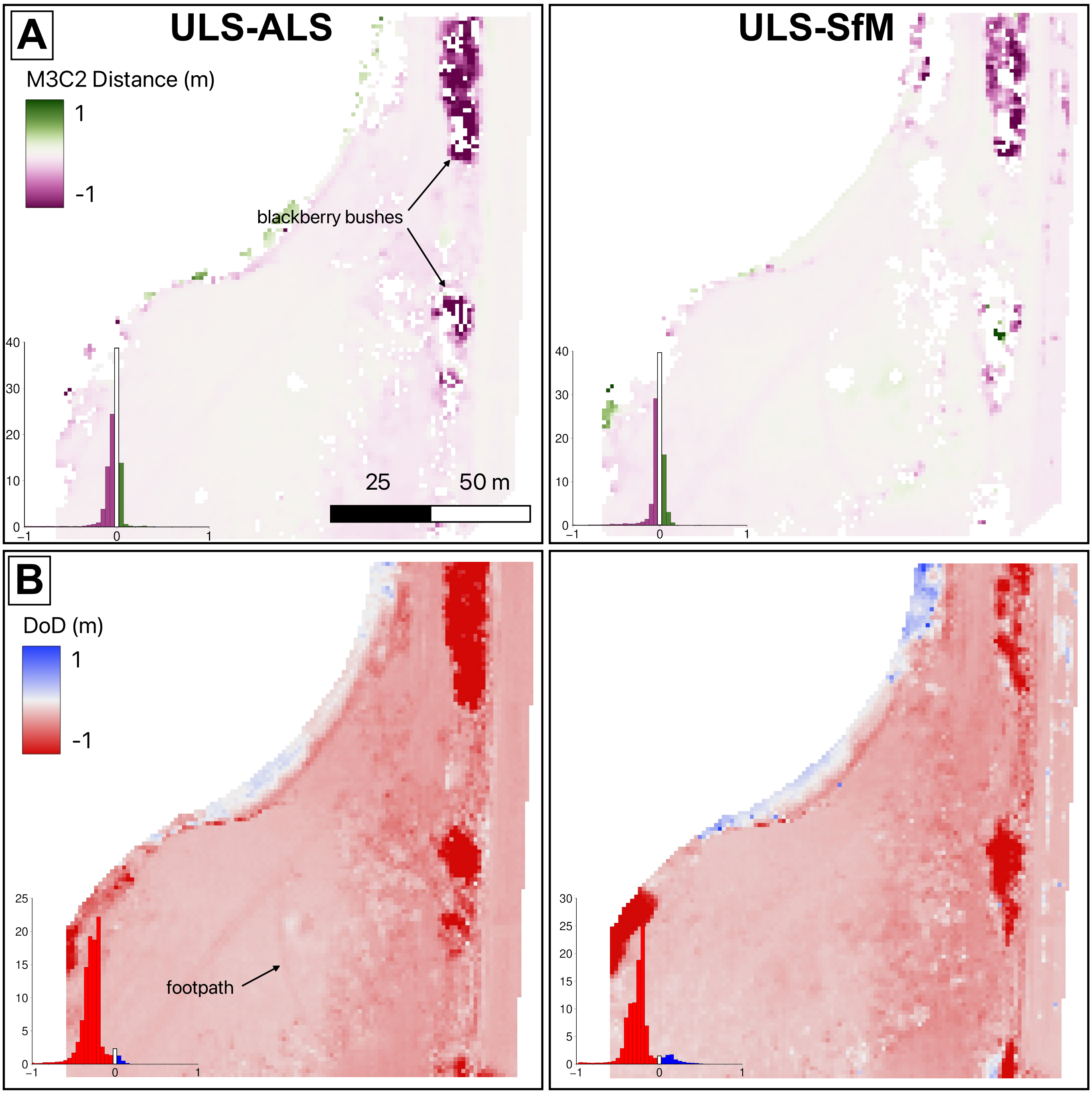

Figure 7 Differencing of the ULS and ALS datasets (left hand column) and of the ULS and SfM datasets (right hand column) at the eastern X̲EOLX̲ELEꝀ (Elk Lake) shoreline site, shown as (A) M3C2 distances calculated in CloudCompare and (B) a DEM of Difference. Positive values indicate where the ULS dataset was higher than the comparison dataset. Histograms show distributions of raster values.

<0.001 radians (Table 3). These values reflect small differences, within the expected error, of the global registration of the two surveys, with minimal tilting of one relative to the other. The mean M3C2 distance between the airborne and drone lidar point clouds was 5 cm with a standard deviation of 19 cm (Fig. 7A, left panel). The equivalent DEM of Difference (DoD) exhibits a mean of −0.32 m and a standard deviation of 26 cm (Figure 7B, left panel). Positive values (blue colours) reflect areas where the ULS DTM is higher than the ALS DTM, and negative values (red colours) reflect those where the ULS DTM is lower. These non-zero values reflect a combination of factors, including residual misalignment of the point clouds (even after ICP co-registration) and internal vertical scatter, estimated from hard, flat, non-vegetated surfaces (e.g. roads, parking lots) at ±6.7 cm in the ALS point cloud and ±7.5 cm in our ULS point cloud. However, careful analysis of the DoD and M3C2 maps also supports a third cause of vertical differences. The largest differences (−2.6 m) were negative and are most likely the result some areas where returns off of dense vegetation were misclassified as ground in either of the datasets. These highest values are approximately in the same area that is covered by dense blackberry bushes (Fig. 5). This also coincides with areas in the airborne lidar that have few to no points (Fig. 6C). It

is likely that the airborne dataset has its lowermost returns from within the blackberry bush rather than the ground surface, while the drone lidar, with its denser point cloud has managed to capture a better ground surface beneath these dense bushes. This also explains why the M3C2 distances are largest in the very same areas.

The ICP rigid body transformation that aligns the ULS and SfM point clouds involved rotations of <0.01 radians and a translation vector of 33 cm, again indicating consistency to within a few decimeters in global registration of the two datasets. The mean M3C2 distance was -0.03 m with a standard deviation of 27 cm (Fig. 7A, right column), while the DoD had a higher mean value of -0.27 m and a standard deviation of 27 cm (Fig. 7A, right column). Given the stark contrast in vegetation penetration capability, it is difficult to interpret these centimetric-to-decimetric differences between the ULS and SfM surveys. Similar to the airborne lidar comparison, the greatest discrepancies are in areas that are covered in dense bushes, where the ULS alone seems to penetrate to ground level.

4 The San Juan fault: a kilometric survey of a fault scarp in steep, forested terrain

4.1 Background and motivations

The San Juan fault (SJF) is a major crustal fault on southern Vancouver Island, located north-west of the XELF (Fig. 2B). The SJF transects the island west to east for $\sim$80 km across densely forested hills of the southern Vancouver Island ranges. In our area of interest, the fault separates the intrusive West Coast Crystalline Complex from the extrusive Jurassic Bonanza Group of the Wrangellia terrane (Harrichhausen et al., 2022). There have been numerous interpretations, inferred from regional geology, of the roles that the SJF has played throughout its evolution (Johnson, 1984; Rusmore and Cowan, 1985; Brandon, 1989; England and Calon, 1991). Most recently, its kinematics have been constrained to have been left-lateral during Eocene accretion of the Crescent-Siletz terrane (Harrichhausen et al., 2022). The position of the SJF in the forearc of the active Cascadia subduction zone, its favourable orientation relative to the regional stress field, and its conspicuously linear trace motivate a close examination of its current activity, but no convincing evidence of recent earthquake rupture has yet been found. If the SJF is active, it may pose a considerable risk to Victoria, Nanaimo, and other towns and infrastructure along Vancouver Island's Highway 1 corridor.

For our drone lidar surveying of the SJF, we targeted a $\sim$4 km section of the fault accessed via logging roads west of Shawnigan Lake (Fig. 8A). The SJF trace is locally defined by a N-facing scarp that appears to cross-cut a glacially scoured surface as well as a number of small tributaries of the Koksilah River. The presence (or absence) of faulted offsets to these glacial and fluvial features could help determine whether this section of the SJF has been active in the late Quaternary. The area of interest includes some steep slopes with a topographic variation of 300 m. Vegetation cover includes stands of second growth Pacific cool temperate forest (Baldwin et al., 2019), with Douglas firs, Western Red Cedars, Western Hemlock and Sitka Spruce trees that are up to 50 m tall. Additionally, some of the area includes recent clearcuts with some small trees and shrubs. Our surveying of the SJF therefore provides good tests both of mapping at kilometric lengthscales over rugged terrain and of the vegetation penetration capability of the drone lidar system.

4.2 ULS data acquisition and results

We surveyed the SJF with our lidar drone in September 2022. For logistical reasons, we split the target area into two sections separated along strike of the SJF by a gap of $\sim$1 km (Fig. 8A). The SJF West section is $\sim$2 km along strike by $\sim$700 m wide and the SJF East section is $\sim$1.7 km along strike by $\sim$700 m wide, with a total surveyed area of 2.9 km^2. The two sites took a total of 2 days to survey (14 hours of field work excluding travel) with a crew of three people (a pilot and two visual observers). The drone was flown at 5 m s^{-1} at a height of 80 m AGL along flight lines oriented parallel to the mapped fault scarp, that were merged with the help of orthogonal calibration lines (supplementary Figures SM2 and SM3). For the SJF-East section, two launch points were required to maintain VLOS around high topography in the center of the survey area. At 80 m AGL the laser footprint is 6.4 cm at the center and 9 cm at the edges of each $\sim$160 m wide swath swath. At each site we deployed 5 GCPs to assist with georeferencing the point clouds.

Our SJF East and SJF West ULS surveys have average point densities of 121 pts/m^2 and 142 pts/m^2 and average classified ground return densities of 11 pts/m^2 (0.3 m spacing) and 17 pts/m^2 (0.24 m spacing), respectively (Table 3). The point clouds are therefore an order of magnitude sparser than those at X̱EOLX̱ELEꝀ (Elk Lake), reflecting the greater platform heights and speeds and reduced swath overlap used in our deployments along the SJF. Additionally, only $\sim$10% of the laser returns along the SJF are classified as ground compared to $\sim$48% at X̱EOLX̱ELEꝀ (Elk Lake), reflecting the stark differences in vegetation between the two target areas. Nevertheless, the drone lidar still captures an abundance of ground surface returns along the SJF, from beneath both mature forest and new growth within clear cuts (Fig. 8C). The optimized 0.5 m-pixel hillshaded ULS DTM captures clearly both the $\sim$E–W-striking fault scarp and several $\sim$NNE–SSW-trending glacial flutes at the SJF West site, as well as the $\sim$NE-trending tributary channels at the SJF East site, one of which exhibits an apparent right-lateral offset at the fault (Fig. 8A). Further analysis and interpretation of this rich dataset will form the basis of future study.

4.3 Comparison and differencing with ALS data

We can compare our ULS data with regional airborne lidar flown for Mosaic Forestry Management in 2021. In

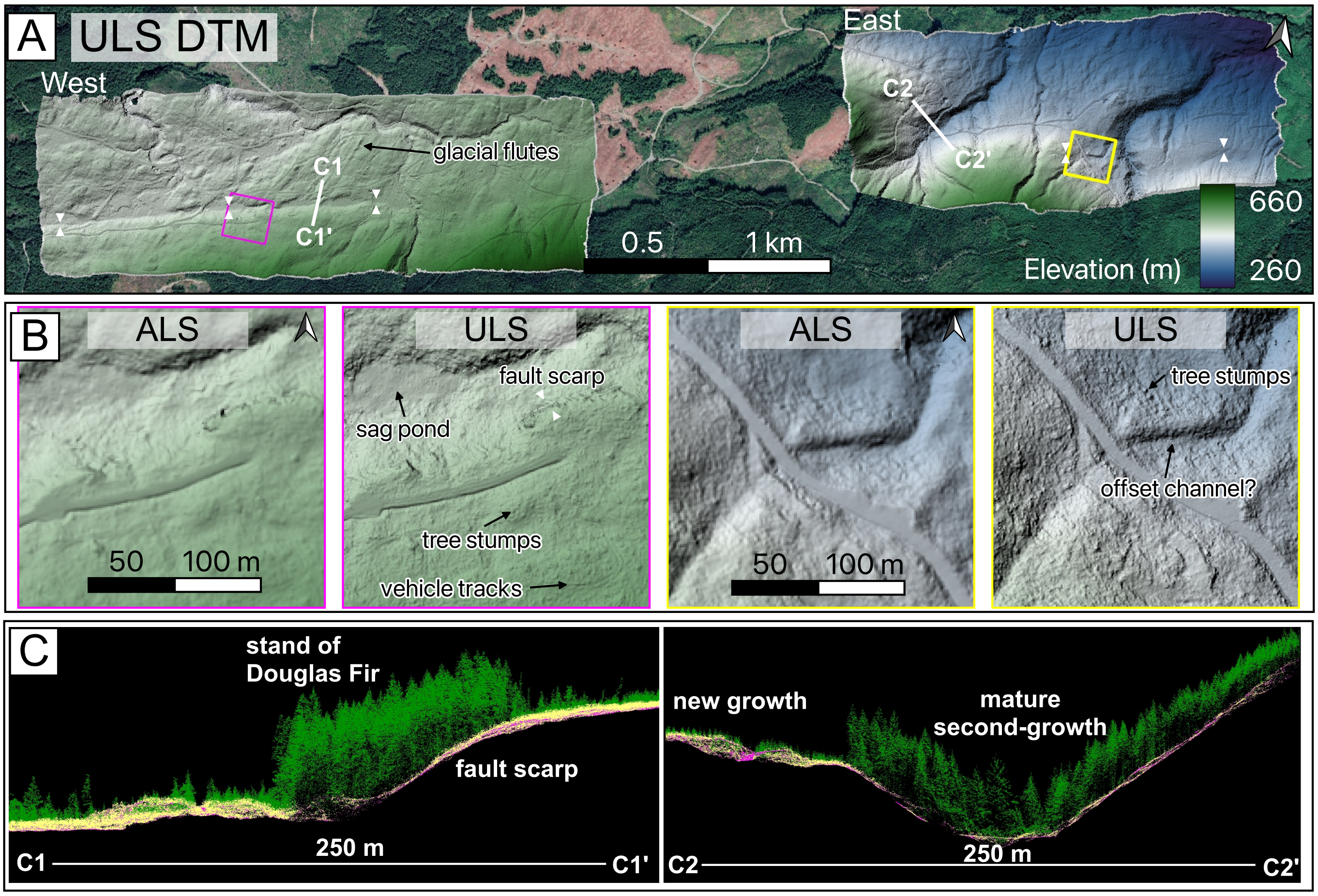

Figure 8 (A) Hillshaded UAV lidar DTM (illuminated from 315°) for the San Juan Fault study area, overlain on satellite photograph. White triangles indicate the approximate location of the SJF. Coloured squares indicate the areas shown in the DTM comparisons below. (B) Comparisons between ALS and ULS DTM hillshades at the SJF West site (left hand panels) and the SJF East site (right hand panels). (C) Cross sections C1–C1' and C2–C2' through the ULS classified point cloud. Green points are vegetation, pink are ground points, and yellow points are unclassified.

the year between the two surveys there appears to have been little forestry activity in the area (and no new cut blocks), allowing a like-for-like comparison. Within the footprint of the ULS surveys, the ALS yields an average ground point density of 6 pts/m^2 and average spacing of 0.43 m, somewhat coarser than the ULS data. A visual comparison of the 0.5 m-pixel ULS DTM with the 1 m-pixel ALS DTM demonstrates how the drone lidar allows for finer scale (<1 m) features to be identified (Fig. 8B). For example, tree stumps and vehicle tracks on clear-cut slopes are clearly visible on the drone lidar hillshade but are only vaguely delineated in the airborne lidar.

The ICP rigid body transformations that best aligned the ALS and ULS point clouds involved rotations of <0.001 radians and translation vectors of 0.07–0.32 m. Post alignment, the average M3C2 distances were 0.22 m for SJF East and 0.13 m for SJF West, with standard deviations of 0.42 m and 0.31 m, respectively, while the equivalent DoDs have mean elevation discrepancies of 0.21 m and 0.15 m with standard deviations of 0.62 m and 0.53 m, respectively (Fig. 9 and Table 3). These results indicate internal consistency of the two datasets to within a few decimeters.

The largest M3C2 distances in the SJF West dataset occur along the northern edge of the ULS survey within a steep valley (Fig. 9A). Our point cloud is sparsest in this area, as it was covered fully by just one flight line. Other small areas with large M3C2 distances highlight where excavations for road maintenance were made between acquisitions (Fig. 9A). There are also small channels that show up as negative values in the M3C2 distance and DoD plots, as a result of improved penetration through dense riparian vegetation in the ULS dataset. The strip of high M3C2 distances in the eastern part of the SJF East dataset results from a mis-aligned ULS flight line, which we discuss further in Section 7.2. In general, the raster differences are a lot noisier than the M3C2 point cloud comparison (Fig. 9B). The largest raster differences are concentrated at the bottom of valleys, areas with both steep slopes and dense vegetation. It is likely that fewer true ground returns were obtained in these areas, but particularly in the ALS dataset, as the ULS dataset generally places the valley floors lower. Similar to the data comparisons undertaken in the previous section, this highlights the better vegetation penetration capability of the drone lidar system.

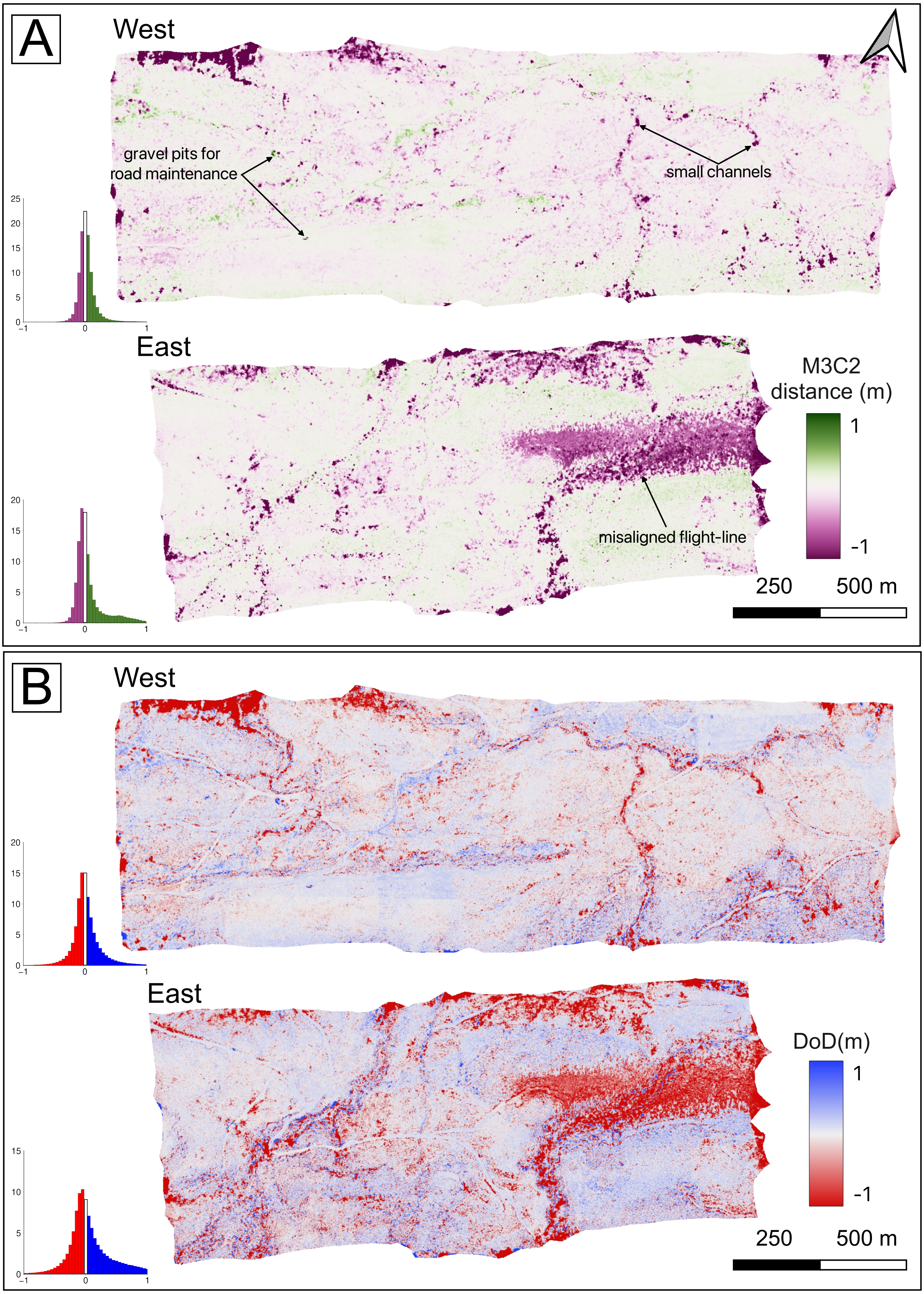

Figure 9 Differencing of the drone and airborne lidar datasets for the SJF study area, shown as (A) M3C2 distances calculated in CloudCompare and (B) a DEM of Difference. Positive values indicate where the ULS dataset was higher than the ALS dataset. Histograms show distributions of raster values.

5 The Southern Rocky Mountain Trench: a kilometric survey of an alluvial fan scarp

5.1 Background and motivations

The Rocky Mountain Trench (RMT) is a conspicuously linear series of NW-trending valleys that crosses the Canadian Cordillera from northern Montana to southern Yukon, where it continues as the Tintina Trench into Alaska (Fig. 2A). It demarcates the boundary between the Omineca and Foreland morphogeological belts and is defined by a series of major fault zones with distinct northern, central and southern segments (Clague, 1975; Gabrielse et al., 1991). The Southern RMT fault (SRMTF), in the East Kootenay region of southeastern BC is a steeply west-dipping normal fault active primarily in the Eocene (van der Velden and Cook, 1996). However, there is some evidence that the SRMTF may remain seismically active (Purba et al., 2021; Finley et al., 2022b), strongly motivating the acquisition and interpretation of lidar data. Our preliminary analysis of newly-released provincial airborne lidar (LidarBC, 2023) revealed a ∼3 km-long, W-facing scarp crossing a series of potentially Holocene-aged alluvial fans above the eastern shoreline of Columbia Lake, just south of the town of Fairmont Hot Springs (Fig. 10A). The exact trace of the SRMTF is not well mapped at this location owing to the thick overburden in the valley floor. However, the scarp is parallel to and aligned with mapped strands of the SRMTF to the north and south, and could potentially indicate a neotectonic reactivation. Given that this part of the RMT was occupied by Glacial Lake Invermere during the late Pleistocene (Sawicki and Smith, 1992), other potential origins including wave-cut shorelines or slumping within weak glaciolacustrine sediments must also be considered.

Our goal in surveying the Columbia Lake scarp with our lidar drone was to help determine its true origin. This includes illuminating any lateral offsets to a series of small runnels that cross the scarp, and characterizing its detailed shape for the purpose of morphologic dating (e.g. Nash, 1980; Arrowsmith et al., 1998; Hilley et al., 2010) or to reveal any bevels that might indicate a compound, multi-earthquake origin (e.g. Zhang et al., 1986; Johnson et al., 2018; Wei et al., 2019). The alluvial fan that constitutes our principle target forms a gently-sloping surface from the western front of the Stanford Range at ∼900–1,000 m elevation to the lake shoreline at ∼809 m. This is covered by a mix of open grassland and groves of ponderosa pine, typical of Cordilleran dry forest (Baldwin et al., 2019). The Columbia Lake site therefore provides a test of our ULS system across a gentler relief and more sparsely-vegetated landscape than along the SJF. Since the survey area lies within traditional territories of the Ktunaxa and Secwépemc First Nations as well as within the Columbia Lake Provincial Park and Nature Conservancy of Canada land, extra research and drone use permissions had to be obtained in addition to the civil aviation approvals described in Section 2.2 (see Acknowledgments).

5.2 ULS data acquisition and results

We surveyed the Columbia Lake site over a period of three days in October 2022 with a crew of two people (the pilot and one visual observer). Our survey covers ∼3.22 km^2, with a length of ∼4 km along strike of the scarp and a width of ∼0.8 km, enough to capture most of the fan surfaces between the mountain rangefront and the Columbia Lake shoreline. The target area was flown in several segments, with orthogonal calibration lines that tie the flights together (supplementary figure SM4). Launch sites were located along the park access road that conveniently runs N–S down the middle of the fan surfaces, often adjacent to the scarp itself. The drone was flown at a height of 80 m AGL and a speed of 4 m s^{-1}, with the gentle relief and mix of grassland and scattered ponderosa pine allowing for excellent sight lines. The ULS data were georeferenced using ten harlequin-iron-cross GCPs.

Our ULS system yielded an average point density of 102 pts/m^2 and was easily able to image beneath the scattered ponderosa pine trees (inset, Fig. 10), producing an average classified ground return density of 36 pts/m^2 at an average spacing of 0.17 m (Table 3). Overall, ∼35% of all laser returns are classified as ground, lower than the ∼48% at X̲EOLX̲ELEK̶ (Elk Lake) but substantially higher than the ∼9% along the SJF, reflecting the differing vegetation densities of the three areas. We optimally gridded the classified ground returns at a pixel resolution of 30 cm (Fig. 10A). The hillshaded DTM clearly reveals the primary scarp striking N–S across the largest, northern alluvial fan (af1), as well as some secondary splays just east of it (Fig. 10D, right panel). It also reveals a lineament within the southernmost alluvial fan (af4) that may represent an along strike continuation of the scarp. We encountered difficulties aligning some of the flight lines due to poor INS calibration, which may explain some N-S linear corduroy artefacts visible in the center of the hillshaded DTM (Fig. 10D, right panel). However, to the trained eye, these minor and localized artefacts are easily distinguished from genuine tectonic landforms.

5.3 Comparison and differencing with ALS data

Our comparison data are provincial airborne lidar collected over a two year period (2015–2017) using multiple sensor platforms with unknown acquisition parameters (LidarBC, 2023). The sparse metadata owe to the fact that these surveys were flown by a third party and later acquired for LidarBC, without the control needed for them to verify accuracies. This captures ∼ 80% of our ULS dataset, but misses the southernmost alluvial fan (af4) surveyed with the drone, where we observe an additional scarp along strike. Within the footprint of overlap, the ALS data have an average ground return density of 7 pts/m^2, five times coarser than the ULS survey, and an average ground return spacing of 0.38 m, twice that of the ULS survey (Table 3). Despite these differences in spatial resolution, there is little visual contrast between the ALS and ULS hillshaded DTMs (Fig. 10D). However, fault-perpendicular topographic profiles reveal that the

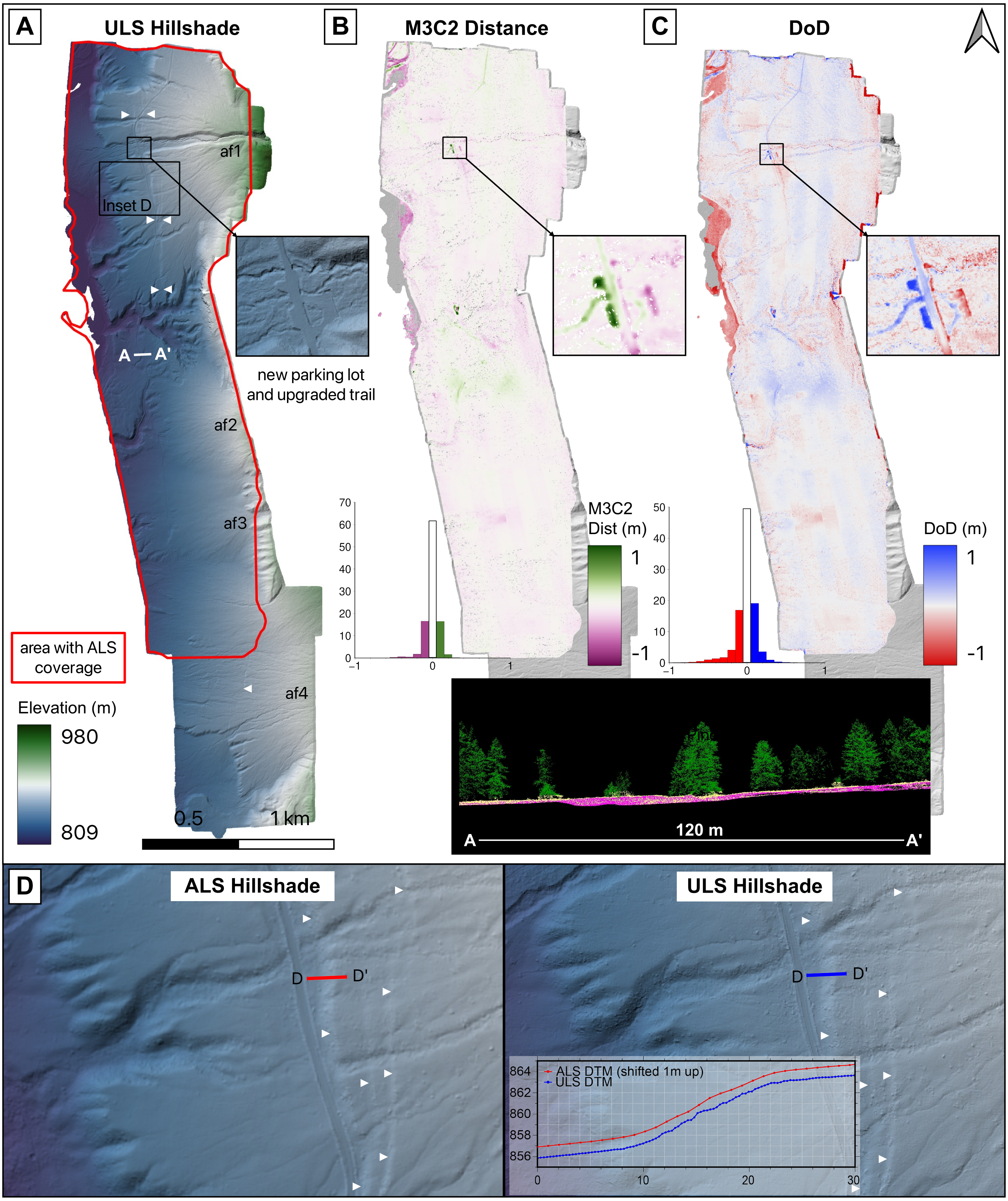

Figure 10 (A) Hillshaded ULS DTM for the Columbia Lake site along the SRMTF. The red polygon shows the area of the ULS survey overlapped by LidarBC ALS coverage. Inset shows the location of a new parking lot and upgraded trail to the lake shore that was not developed when the provincial lidar was collected. Alluvial fans (af) are numbered from northernmost (af1) to southernmost (af4). White triangles indicate the approximate location of the SRMTF. (B) M3C2 distances between the ULS and ALS point clouds, with an inset showing changes over the new parking lot and trail. Positive values indicate where the ULS dataset was higher than the ALS dataset. (C) DoD (ULS-ALS), with an inset showing changes over the new parking lot and trail. The inset below (C) and (D) shows cross section A—A' through the classified drone lidar point cloud, with green points for vegetation, pink for ground points, and yellow for unclassified returns. (D) Comparison between ALS and ULS hillshaded DTMs. Cross section D-D' shows the increased level-of-detail in the ULS DTM along the main scarp. Note that the ALS profile has been shifted upwards by 1 m in order to aid comparison.

shape of the scarp is captured by ULS at greater detail than by ALS (inset to Fig. 10D).

The ICP rigid body transformation that most closely aligns the two point clouds has a translation vector of 0.54 m and a rotation of <0.001° (Table 3). After this global registration, the mean M3C2 distance between the aligned point clouds is -0.01 m with a standard deviation of 0.09 m, while the DoD has an average elevation difference of -0.02 m with a standard deviation of 0.29 m. These results show that despite some artefacts (described below), our ULS dataset is still both aligned to within a few decimeters and internally consistent to within a few centimeters with the ALS survey.

The greatest differences between the two point clouds as revealed by M3C2 and DoD maps (Fig. 10 B–C) are along the park access road: a gravel pit in the south and a parking lot in the north, both of which we suspect were excavated or re-graded between surveys. There are also negative M3C2 and DoD values along the Columbia Lake shoreline, which likely represent changing water levels between acquisitions. However, the M3C2 distance and DoD plots also highlight alternating N–S strips of negative and positive values (± 15 cm), clearest in the northern half of the survey. We interpret these as errors in the ULS point cloud due to a poorly calibrated INS on some of our flights.

6 The Eastern Denali fault: maximal coverage of a major strike-slip fault

6.1 Background and motivations

The Denali fault hosted North America's largest and longest onshore earthquake of the modern instrumental period. The M_w 7.9 earthquake of November 3 2002 ruptured for $\sim$340 km west to east across central Alaska, producing mostly right-lateral surface offsets of up to $\sim$9 m (Eberhart-Phillips et al., 2003). Though the Denali fault continues southeastwards into Yukon and northwestern BC (Fig. 2A), the 2002 earthquake stopped short of the Canadian border, branching instead onto the Totshunda splay fault, where it terminated. This rupture pattern has elicited investigations into the current activity and kinematics of the Denali fault east of the Totshunda junction (Bostock, 1952; Clague, 1975; Haeussler et al., 2017; Marechal et al., 2018; Blais-Stevens et al., 2020; Choi et al., 2021), usually referred to as the Eastern Denali fault (EDF). The EDF has been active in the Holocene since it lacks a glacial overprint and displays several push-up or mole-track structures within till (Bostock, 1952; Blais-Stevens et al., 2020). Paleoseismic trenching of the fault and coring of lake sediments ponded against the scarp also revealed evidence for five strong earthquakes during the past $\sim$6,800 years, leading Blais-Stevens et al. (2020) to call for the acquisition of lidar imagery to better illuminate the surface offsets, kinematic style, and other characteristics of these events.

We targeted a $\sim$100 km stretch of the EDF centered upon Lù'àn Män (Kluane Lake) and paralleling the paved Alaska Highway (Fig. 11D). This section of the fault occupies a broad glacial valley, surfacing up to a few kilometers NE of the frontal range of the St. Elias mountains and displays tectonic landforms including those targeted for paleoseismic trenching and coring by Blais-Stevens et al. (2020). The area is mostly covered by boreal forest (Fig. 2A), consisting mainly of white spruce trees, aspen and balsam poplar. However, the EDF crosses several wide fluvial terraces deposited by rivers sourced in the St. Elias mountains, the youngest of which are only sparsely vegetated. Our work along the EDF therefore provides an example of surveying rugged (though not mountainous) topography containing both dense and sparse vegetation. Our surveying of the EDF also represents our closest attempt at a regional ULS survey. We sought to survey as much of the fault as possible, but sparse secondary road coverage off the main Alaska Highway prevented us from accessing long stretches of it. We therefore flew several separate sections of the EDF from launch sites located wherever a passable road crosses the fault, usually one that follows a major river sourced in the St. Elias mountains (Fig. 11D). However, these river outlets are also where we expect to observe some of the best expressions of the fault in Quaternary deposits, such as deformed river terraces and offset terrace risers. Our drone coverage, though discontinuous, should therefore still capture many of the features of greatest geomorphic interest.

6.2 ULS data acquisition and results

We collected $\sim$10 km^2 of drone lidar data at seven individual survey sites—from NW to SE, Quill Creek, Burwash Creek, Duke River, Copper Joe Creek, Nines Creek, Slims River/Topham Creek, and Telluride Creek—that together capture a $\sim$15 km length of the EDF (Fig. 11D). Data were acquired during two, week-long field campaigns in September 2021 and August 2022, each involving three crew members (a pilot and two visual observers); the largest site, at Duke River, was flown over multiple days (Fig. 11A). Flight paths for each site are plotted in supplementary figures SM5–SM11. The drone was flown at 80 m AGL and speeds of 5 m s^{-1} in 2021 and 4 m s^{-1} in 2022. Since large portions of each target area were difficult to access on foot, we were unable to deploy as many GCPs as we did at the study sites described in previous sections. The number of GCPs range from 2 at the Nines and Quill Creek sites to 20 at the Duke River site (cumulative across several days of surveying).

The seven ULS surveys yielded average point densities of 80–112 pts/m^2 with a mean of 98 pts/m^2, average classified ground return densities of 20–72 pts/m^2 with a mean of 45 pts/m^2, and average ground return spacings of 0.19–0.23 m with a mean of 0.21 m (see Table 3 for results of each individual survey). Generally, the ULS does an excellent job of imaging beneath the boreal forest canopy (inset, Fig. 11A), with $\sim$47% of all laser returns classified as ground. We did encounter some misalignment of flight lines in some of the datasets—particularly at Quill Creek—again, potentially due to a poor INS calibration. This can produce some striping in the M3C2 and DoD results (Fig. 12), with separations of ± 15 cm in places. However, these linear artefacts are easily distin-

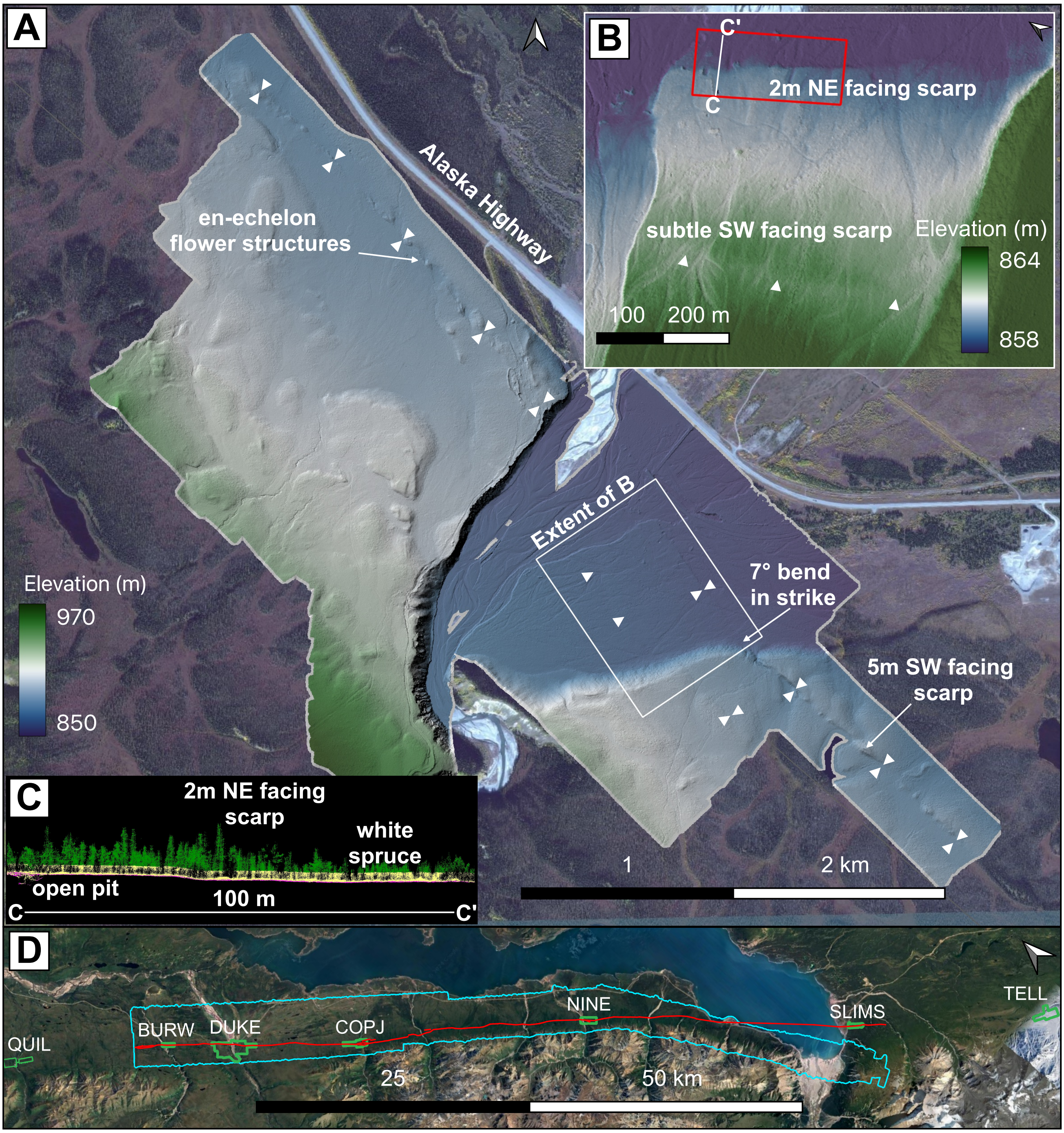

Figure 11 (A) Hillshaded drone lidar DTM of the Duke River site on the Eastern Denali fault (EDF). The extent of panel B is marked by the white rectangle. White triangles indicate the approximate location of the EDF. Underlying satellite imagery is from Bing. (B) Inset showing a 2 m high northeast facing scarp along a river terrace. The red polygon shows the bounds of the flight parameter testing discussed in Section 7.1. White line shows the location of cross section C–C'. (C) Cross section C–C' through the classified ULS point cloud, with green for vegetation, pink for ground returns, and yellow for unclassified points. (D) Locations of all ULS collection sites (green polygons) along the trace of the EDF as identified with lidar data (red line). The cyan polygon outlines the comparison ALS dataset. Satellite imagery is from Google. QUIL = Quill Creek, BURW = Burwash Creek, DUKE = Duke River, COPJ = Copper Joe Creek, NINE = Nines Creek, SLIMs = Slims River/Topham Creek, TELL = Telluride Creek.

guished from genuine tectonic landforms. The ground returns were rasterized at an optimal pixel resolution of 0.3 m for each of the seven individual surveys.

We focus our further analysis in this paper on the Duke River site, which is the largest and densest of our EDF ULS surveys (Fig. 11 and Table 3). Results from the other EDF drone lidar surveys are presented in the supplemental material (SM14—16); some of them were also interpreted in an earlier technical report of ours (Finley et al., 2022a) and a full tectonic analysis of all

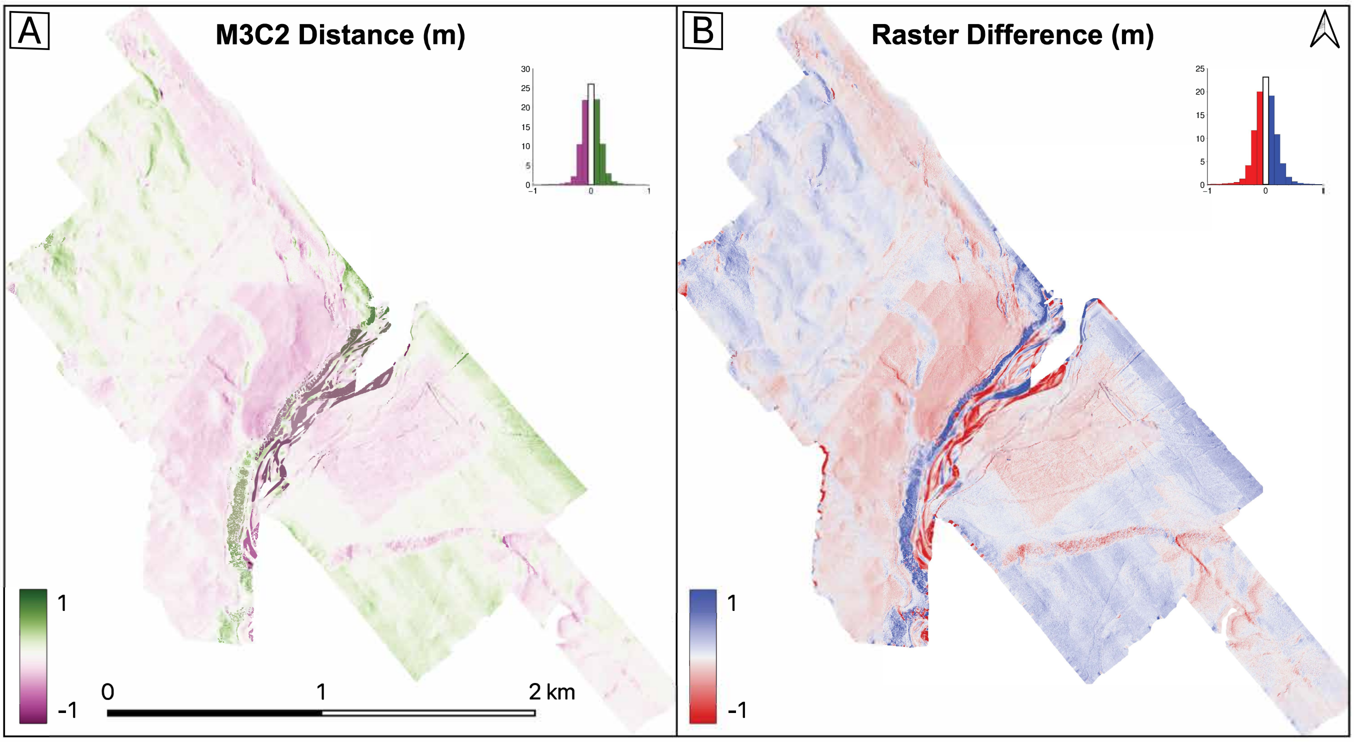

Figure 12 Differencing of the drone and airborne lidar datasets for the Duke River site along the EDF, shown as (A) M3C2 distances calculated in CloudCompare and (B) a DEM of Difference. Positive values indicate where the ULS dataset was higher than the ALS dataset. Histograms show distributions of raster values.

of the EDF lidar topography will be the subject of a future paper. The 0.3 m-resolution Duke River DTM showcases several interesting tectonic landforms along the principal trace of the EDF (Fig. 11A). From NW to SE, these include en-echelon push up structures indicative of dextral strike-slip, a pair of clear, right-lateral offsets to terrace risers south of the active Duke River, an abrupt, 7° bend in fault strike, and a large, SW-facing scarp with a vertical separation of ~5 m. The lidar DTM also reveals a previously unmapped, secondary strand of the EDF, expressed as a SW-facing scarp crossing the widest, southern terrace of the Duke River (Fig. 11B). This highlights the potential for drone lidar to capture subtle, off-fault tectonic landforms away from principal fault traces.

6.3 Comparison and differencing with ALS data

Until this study, the Canadian portion of the Denali fault had not been flown systematically with lidar, with the best freely-available topographic data coverage being the 2 m-resolution, satellite photogrammetry-derived ArcticDEM (Morin et al., 2016) and a bespoke 4 m-resolution DTM constructed from legacy airphotos using SfM (Bender and Haeussler, 2017). In addition to our drone lidar surveying described above, one of us (B.M.) also collected a ~295 km^2, ~70 km-long airborne lidar swath on 19 August 2018 that captures ~50 km of the EDF between Burwash Creek and south of Nines Creek (Fig. 11D), which for the purposes of this study we use as our comparison dataset. The ALS survey covers four of our seven drone lidar sites, including the largest at Duke River. The airborne lidar yields an average point density of ~8 pts/m^2 and an average ground return density of ~3.5 pts/m^2, less than 10% of the equivalent ULS values, and the average ALS ground return spacing is 0.54 m, more than double that of the ULS (Table 3). Consequently, the ULS DTM exhibits noticeably finer detail than is discernible in the ALS DTM.

For the Duke River dataset, the ICP rigid body transformation that optimally aligns the ULS and ALS point clouds has a translation vector of 0.54 m and a maximum rotation of 0.0003°, indicating global registration to within a few decimeters and negligible tilting (Table 3). The mean M3C2 distance between the aligned point clouds is 0.00 m with a standard deviation of 0.18 m, while the DoD has an average elevation difference of 0.00 m with a standard deviation of 0.28 m, indicating excellent internal consistency between the two lidar surveys. The other survey sites with paired coverage have slightly higher global ICP translations (of up to 0.99 m), but had similarly low mean M3C2 and DoD values (of up to 0.01 m) and standard deviations (of up to 0.28 m).

After ICP alignment of the ULS and ALS ground returns, the largest M3C2 distances between the two clouds are along the active braided channels of the Duke River, with some showing erosion and others deposition such as from the formation of sandbars (Fig. 12A). There are also some large M3C2 distances found along the bluffs on the northern bank of the Duke River. These steep slopes are mostly composed of unconsolidated glacial till and are very unstable, with several small failures occurring while we were working in the area. Thus, it is unsurprising that there are differences in these surfaces between the ALS and ULS acquisitions. Other areas with non-negligible M3C2 values may result from slight misaligments between the individual, day-to-day acquisitions at the Duke River site, which were georeferenced using separately-surveyed GCP deployments. The raster DoD highlights similar areas of difference (Fig. 12B), although it does appear a little noisier than the M3C2 distances due to small misalignments in the rasterization of roads, small channels and other linear features.

7 Discussion

7.1 Flight parameter trade-offs

The four case studies described in Sections 3–6 highlight not only the usual trade-off in remote sensing between data spatial resolution and coverage, but also the flexibility in drone surveying to adjust flight parameters for the job at hand in a way that would be difficult with a crewed aircraft platform. For example, for our local survey of the eastern X̱EOLX̱ELEꝀ (Elk Lake) shoreline site, we flew the drone at a substantially slower speed and a lower height than in the other, kilometric-scale surveys, resulting in a point cloud that was around five times denser but also smaller in scale (Table 3). In practice, however, the trade-off between platform speed and point cloud density is complicated by the limited battery life of the drone, which restricts the area that can be collected in a single flight.

We therefore conducted an explicit test of the trade-offs between platform speed, flight duration, and lidar point density, with the aim of determining the ideal flight parameters for collecting high-density data as efficiently as possible. We did so during our surveying along the EDF in 2022, choosing for the test a small (∼2500m^2) area of the Duke River site centered along a segment of the EDF that offsets an abandoned, forested river terrace (Fig. 11B). We surveyed this area nine times over the course of a single day, at 1 m s^{-1} increments in speed from 1 m s^{-1} to 10 m s^{-1}, using the same optimal flight height (80 m AGL) and the same flight pattern (Fig. 13B, left panel). The nine flights yielded order of magnitude ranges in both point densities, from ∼51–496 pts/m^2, and classified ground return densities, from ∼10–68 pts/m^2 (Table 4). We observe the expected tradeoff between platform speed and ground return density, with the slowest flight yielding more than double the point density of the next slowest flight but taking double the time (Fig. 13A). The resulting DTMs all looked similar to the eye (Fig. 13B), although the data from faster collections were slightly noisier. The faster collections had a greater variation in the DTM surface, potentially as a result of small bushes and other low vegetation being classified as ground.

Ultimately, the most efficient speed for a given survey depends on the desired point density and should be determined on a case-by-case basis accounting for both the scale of the features being targeted and the vegetation cover type. In our general case, we strive for submeter pixel DTMs in order to identify fine-scale fault geomorphology that might not be visible in existing airborne datasets. Ideally, each raster cell value should be based on the average of at least 3 ground returns. Thus, for a 50 cm DTM, 12 ground returns per square meter are desirable, allowing each raster cell to be calculated using a minimum of 3 ground points. The minimum DTM resolution in Table 4 was calculated using this rule of thumb. Using Fig. 13A as a guide, an appropriate maximum acquisition speed would therefore be about 6 m s^{-1}. Anecdotally, this agrees well with our experience gleaned from many drone lidar campaigns.

7.2 Drone lidar performance

Our four case studies described in Sections 3–6, as well as the additional testing at the Duke River site described above, demonstrate the wide range of ground return densities attainable with drone lidar, governed principally by the platform height and speed, swath overlap, and vegetation type. At its densest—our local survey of a planned paleoseismic site along the XELF with only scattered tree cover (Section 3)—we obtained a ground point density of 260 pts/m^2 at an average spacing of 6 cm, though of course further improvements would have been possible with additional, overlapping flight lines. In surveys undertaken at the kilometric length scales more generally of interest to tectonic geomorphologists, we obtained ground return densities ranging from ∼10 pts/m^2 (spacing of ∼30 cm) along the rugged, heavily forested SJF (Section 4) to ∼70 pts/m^2 (spacing of ∼20 cm) at the mixed-cover Duke River site on the EDF (Section 6). In all cases, the ULS densities were a marked improvement from those of the comparison ALS datasets, which ranged from 3.5–9 pts/m^2 with spacings of 0.33-0.54 m (Table 3). Of course, these differences trade off against aerial coverage; in our largest ULS survey along the EDF we collected a total of ∼10 km^2 of data in two week-long field campaigns, whereas our ALS survey collected 25 times that area in a single day. Our ULS surveying along the SJF, SRTM and EDF shows that coverage of 0.5–1.6 km^2 is achievable in a single day with the drone, including over rugged topography.

Our ICP alignments of ULS ground returns with corresponding ALS point clouds show that the two datasets are usually globally registered to within less than a meter of one another (Table 3), with the one exception, along the SJF, likely arising from differences in the geoid model used to calculate orthometric heights (Section 4.3). The Riegl MiniVUX-1UAV laser scanner has expected accuracy of 10 mm and precision of 5 mm and the Applanix APX20-UAV INS has a post-processed accuracy of 2–5 cm. Once the ULS and ALS ground return clouds are aligned using ICP, average M3C2 distances and DoD values on the order of a few centimeters are therefore within the expected noise, especially considering that the average is biased by localized occurrences of significant landscape alteration between surveys (e.g. road construction; Fig. 10B–C). Generally, the M3C2 distances were very similar to the DoD values, implying that the local distances calculated on the point clouds were mainly in the vertical direction. We did encounter artefacts arising from misaligned flight lines within some of the ULS datasets (e.g. Figs. 7B and 9), al-

Speed ($m\ s^{-1}$)	*Survey time (min)*	*Point density (pts/m^2)*	*Ground point density (pts/m^2)*	*%pts ground*	*Minimum DTM resolution (m)*
1	23.50	495.63	68.36	14	0.21
2	11.75	242.49	28.16	12	0.33
3	7.83	155.68	23.80	15	0.36
4	5.88	122.87	20.10	16	0.39
5	5.37	99.83	19.20	19	0.40
6	4.47	84.98	15.58	18	0.44
7	3.83	72.70	12.12	17	0.50
8	3.35	65.17	14.19	22	0.46
9	2.98	57.93	9.70	17	0.56
10	2.68	50.52	10.05	20	0.55

Table 4 Results of our testing of platform speed trade-offs. The survey time does not include the static IMU calibrations (∼5 minutes per flight), nor the time taken to transit the drone between the launch site and the start of the first data collection flight line. The minimum DTM resolution is based on a recommendation that at least 3 ground points should be averaged per raster cell.

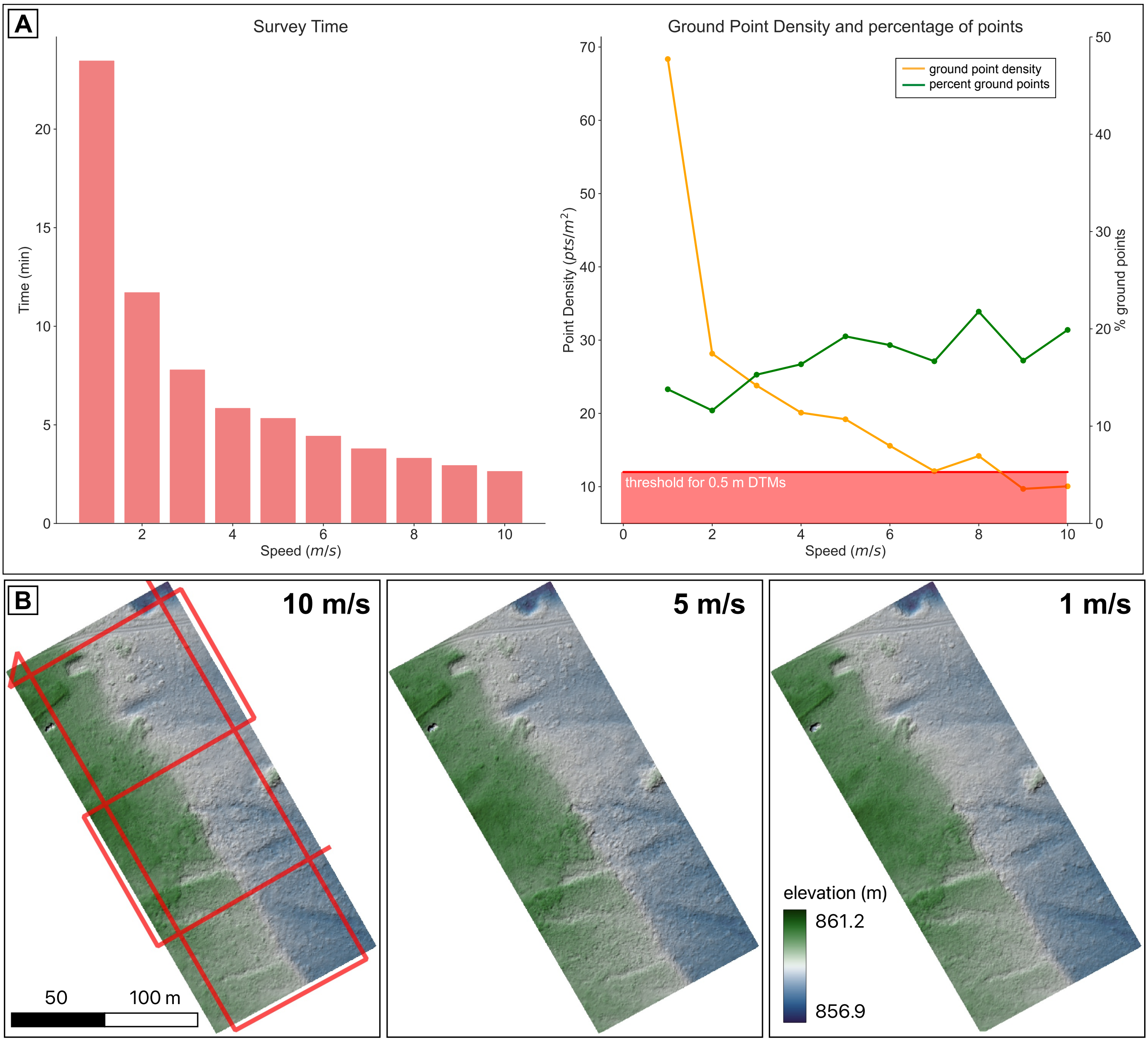

Figure 13 Results of platform speed trade off tests. (A) Relationships between acquisition time, platform speed, and the resulting ground return density. The 12 points per square meter threshold illustrates that sub-0.5 cm DTMs can only reliably be obtained at speeds of 6 m s^{-1} or less. (B) 30 cm-resolution DTMs for the fastest (10 m s^{-1}), intermediate (5 m s^{-1}) and slowest (1 m s^{-1}) flights. The red line on the 10 m s^{-1} panel shows the acquisition path used for all flights.

though further post-processing may have helped reduce these (Gu et al., 2023) and similar problems can occur in some ALS surveys, too (Scott et al., 2022). One main challenge for mobile lidar systems thus far has been in point accuracy, particularly as a result of the IMU trajectory Glennie et al. (2013), and our ULS results bear this out.

Our detailed comparisons of data collected at the eastern X̱EOLX̱ELEꝀ (Elk Lake) shoreline site show how ULS penetrates low-lying vegetation (blackberry bushes) better than ALS does, with both lidar systems naturally outperforming SfM (Section 3.3). Counterintuitiuvely, the ULS produces a lower fraction of ground returns (48%) than the ALS (64%), which hints that in densely-vegetated areas, some laser returns off shrubs and bushes might be misclassified as ground in ALS datasets, to a greater extent than they are in ULS datasets. This would explain why the ground surface modelled from ULS data is often slightly lower than that from ALS data (Figs. 7 and 9). It is important to note that many ground classification algorithms, such as progressive morphological filters (Zhang et al., 2003) and cloth simulation functions (Zhang et al., 2016), were developed using and for ALS data. Thus to effectively determine ground points within ULS data, the default algorithm parameters may need to be adjusted.

The relative vegetation penetration capabilities of ULS and ALS are further showcased in Figure 14. In the left-hand column, we plot 5 m wide point cloud swath cross-sections for typical vegetation present in each of the study sites. These demonstrates that the ULS is better at both capturing the vegetative structure and minimizing gaps in the ground returns. This may partly reflect that the ULS footprint is ∼6–9 cm in diameter at our optimal flight elevation of 80 m AGL, several times narrower than the ∼15–90 cm footprints typical of airborne systems (e.g. Lin et al., 2013; Fernandez-Diaz et al., 2014).

Tectonic geomorphologists generally analyse rasterized DTMs rather than point clouds and so it is important to consider ULS in this context. The ∼1–10 pts/m^2 ground return densities typical of ALS data (Figure 14, middle column) usually translate to ∼1 m raster resolutions, whereas the much the denser point clouds collected by our drone system (Figure 14, right-hand columns) allow for finer pixel dimensions of 0.2–0.5 m. Lin et al. (2013) proposed that 0.5 m was an optimal DTM resolution for detecting tectonic-geomorphic signals, with 0.25 cm pixels offering little improvement, but this may reflect the larger (0.41 m) footprint of their airborne laser scanner. Since ULS laser footprints are much smaller (6–9 cm), it enables us to produce sub-50 cm DTMs which aid the identification of many features obscured in typical 1 m resolution imagery, such as ruts in road-ways, footpaths, and individual tree stumps or logs (e.g. Figs. 7 and 8B).

7.3 Limitations and future prospects of drone lidar

Based on our four case studies in Sections 3–6 and the performance metrics discussed above, we foresee a number of specific applications for drone lidar within the field of tectonic geomorphology. Because battery life, road access, and VLOS requirements limit us to kilometric fault length-scales (e.g. Fig. 11D), we do not envisage ULS (or any other type of drone-based imaging) as a regional reconnaissance tool in the way that ALS has become. However, ULS may be a useful, relatively low-cost way of extending lidar coverage beyond the footprint of an existing ALS survey, such as we did along both the SRMT and EDF (Figs. 10A and 11D). As demonstrated in Section 3 and 7.2, ULS also offers better and more even ground point coverage beneath trees and shrubs than ALS, making it possible to densify lidar coverage along known faults in vegetated landscapes. Faulted landforms targeted for paleoseismic trenching, slip rate studies, or morphologic dating may benefit from the finer, decimetric spatial resolutions achievable with ULS. We have also shown how drone lidar can reveal subtle landforms associated with structural complexity and distributed deformation, such as the secondary scarps imaged on the Columbia Lake alluvial fans (Fig. 10D) and at the Duke River site along the EDF (Fig. 11). There is also scope for mapping landscapes and landforms associated with other natural hazards, such as landslides (Pellicani et al., 2019), volcanoes, tsunamis, and flooding. Finally, because drone deployments are both logistically easier and cheaper than procuring a crewed aircraft, there is rich potential for the use of ULS for rapid response (e.g. mapping of new earthquake surface ruptures) and in repeat mode (e.g. high temporal and spatial resolution time-series of postseismic afterslip). Building upon this study, the capability of repeat ULS surveying for mapping three-dimensional surface deformation will be tackled explicitly in a forthcoming paper of ours.

Just as ULS will complement rather than supplant ALS as a source of high-resolution topographic data, we do not see it replacing TLS or drone-based SfM systems for all applications. Firstly, the upfront costs of our ULS system (discussed further below) are higher than that of many TLS systems and much higher than those of drone-based SfM. Since many consumer drones come equipped with high-quality cameras (e.g. Pellicani et al., 2019), we envisage that SfM will remain the tool of choice for collecting high-resolution topography in arid, vegetation-sparse landscapes (e.g. Johnson et al., 2014). ULS would still offer certain advantages over SfM in such regions—for example its active source allows mapping in low light conditions, and the processing of the lidar point cloud is significantly less computationally intensive—but these would come at greatly increased cost. Similarly, ULS is unlikely to replace TLS for applications in which ground-based scanner vantage points suffice. However, ULS can capture a small target area quicker than TLS; for example, Brede et al. (2017) collected a 140 pts/m^2 ULS dataset in a single 9 minute flight, whereas it took two days to complete TLS coverage of the same 100 m × 180 m site.

The components of our ULS system cost more than CAD $100,000 when purchased in 2018–2019, though these costs are likely to decrease significantly as the technology matures (e.g. Van Tassel, 2021). As ULS is

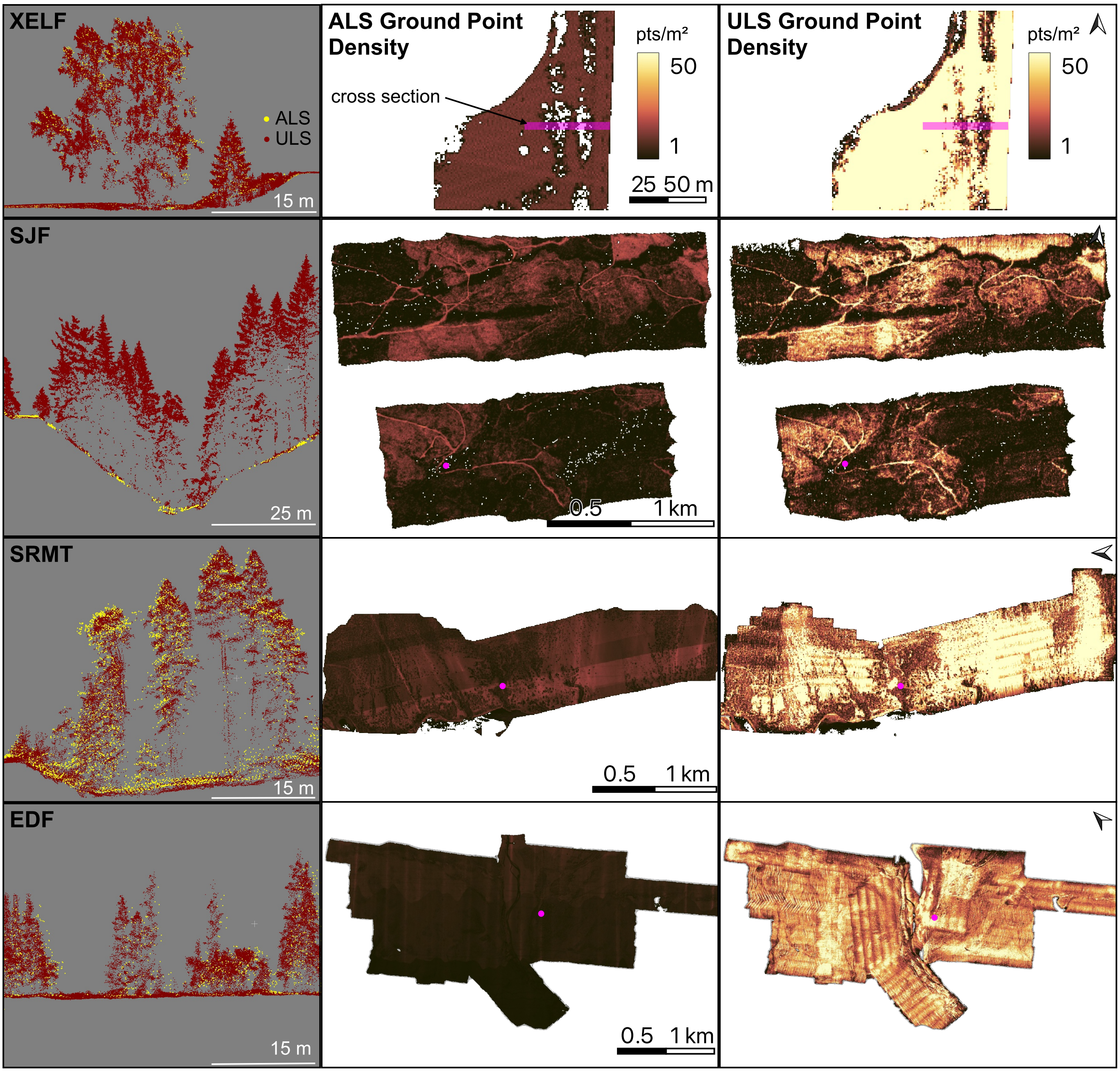

Figure 14 Left-hand column: representative 5 m-wide swath cross-sections through the ULS (red) and ALS (yellow) point clouds showing typical vegetation for the XELF (top row), SJF (second row), SRMT (third row) and EDF (bottom row) study sites. The point clouds are displayed concurrently, with ALS points enlarged to prevent them from being obscured behind ULS points. Note that for the SJF site, only ALS ground returns were provided to us. Middle column: ground point density maps for the ALS datasets at the four study sites. Pink polygons mark the cross-section locations of the left-hand column. Right-hand column: ground point density maps for the ULS datasets. Additional ULS point cloud profiles through stereotypical vegetation for each survey site are provided in supplemental figures SM17—20.

adopted for a broader range of scientific and commercial applications, an increasing variety of drones and miniaturized scanners and INS instruments are becoming available, including as part of integrated systems. In our experience, once the upfront costs of purchasing a ULS system is made, the year-on-year costs for insurance and software licensing are inexpensive. One of the biggest constraints on drone systems is their limited flight time, related to battery life. However, electric cars and a growing array of battery powered mobile devices are driving improvements in battery technology that will positively benefit drone surveying (Townsend et al., 2020; Liang et al., 2019; Rajashekara, 2013, e.g.). Alternatively, gasoline and hybrid-powered UAVs are becoming commercially available, offering much higher energy densities and ensuing improvements in both flight time and lifting capacity (e.g. Skyfront, 2023; Metcalf et al., 2022; Viswanathan et al., 2022; Harris Aerial, 2023). Another major constraint for ULS is imposed by aviation authorities, which require specialist equipment and large amounts of permitting for beyond visual line-of-sight (BVLOS) flight in both Canada and the U.S. Flying BVLOS would allow for larger drone acquisitions with fewer crew and less time in the field. This will potentially change as drone software and collision avoidance systems mature and new RPAS-specific legislation emerges (Transport Canada, 2023).

8 Conclusions

We describe a state-of-the-art drone lidar system, provide a practical guide for other researchers interested in developing their own, and showcase its performance using four case studies from a range of terrain and vegetation types found within the Canadian Cordillera. These range from a local ($\sim$100 m × 100 m) survey of a paleoseismic trenching site with scattered tree cover, captured at a ground return density of 260 pts/m^2, to multi-kilometer mapping of faults in remote, forested regions, captured with ground return densities of $\sim$10–72 pts/m^2. Our ULS point clouds are gridded into bare earth DTMs with $\sim$20–50 cm pixel dimensions, substantially finer than the $\sim$1 m dimensions typical of airborne lidar DTMs. In most cases, the drone lidar ground returns are globally registered to overlapping airborne lidar data to within $\sim$0.3–1.0 m, and once aligned, point-to-point distances and DEMs of difference indicate internal consistency to within a few centimeters. Distinct advantages of terrain mapping using ULS include better imaging beneath vegetation, the flexibility to adjust flight parameters to achieve a desired ground return density, and relatively straightforward platform deployment logistics. In practice, ULS mapping is currently limited to kilometric lengthscales by battery life, road access requirements, and regulatory constraints, so it is unlikely to replace ALS for regional fault reconnaissance. However, we envisage rich potential of drone lidar for (1) cost-effectively mapping faults beyond the edges of existing ALS surveys; (2) detailed surveying of known faults for paleoseismic trenching, fault slip rate estimations, or morphologic dating; (3) revealing subtle landforms arising from off-fault deformation; (4) rapid collection of perishable data such as along earthquake surface ruptures; and (5) for repeat deployments along surface ruptures for capturing afterslip.

Acknowledgements

We are grateful to have conducted this work on the traditional territories of the W̱SÁNEĆ people (XELF), the Hul'q'umi'num speaking people (SJF), the Ktunaxa and Secwépemc (SRMT), and the Lù'àn Män Dän (Kluane Lake People, EDF). Our ULS system was supported through the Canada Foundation for Innovation John Evans Leadership Fund (CFI JELF) and the Government of British Columbia Knowledge Development Fund (BCKDF), and we also acknowledge generous educational discounts and in-kind contributions from Riegl, Applanix, Candrone, and Cansel. Fieldwork in BC was primarily supported by the Natural Sciences and Engineering Research Council of Canada (NSERC) through Discovery Grants #2017-04029 and #2019-05639 (to E.N. and B.M. respectively) and fieldwork in the Yukon by the Yukon Geological Survey. G.S. was supported in part through an Agnew Memorial Scholarship from the University of Victoria, T.F. through an NSERC Alexander Graham Bell Canada Graduate Scholarship, and E.N. and B.M. through Canada Research Chairs. We thank Chris Bone at University of Victoria's Department of Geography for sharing lab space, equipment, and running costs so generously. We are grateful to Chris Crosby for facilitating the hosting of our drone lidar data on the OpenTopography web portal, which is supported by the National Science Foundation under NSF Award Numbers 1948997, 1948994 and 1948857. We thank the Capital Region District (in particular April Mitchell, Jeannette Mollin and Marc Solomon) for allowing us to work within the Elk/Beaver Lake Regional Park, BC Parks for granting us access to Columbia Lake Park, the Yukon Geological Survey (in particular Maurice Colpron, Carolyn Relf and Sarah Sternbergh) and the Arctic Institute of North America's Kluane Lake Research Station for facilitating fieldwork along the EDF, and Mosaic Forest Management for sharing airborne lidar data along the SJF and for granting us access to field sites there. We also thank our University of Victoria colleagues Israporn Sethanant, Élyse Gaudreau, Jinrui Liu, and Braeden Clark for their assistance as visual observers during our drone surveys, as well as Andrew Schaeffer, Lucinda Leonard, Eva Kwoll and John Cassidy for their suggestions and support of the project. Finally, we are grateful to Nadine Reitman, Randy Williams, and an anonymous reviewer for their thoughtful comments that improved the manuscript.

Data and code availability

Supplemental material can be found on Zenodo (https://doi.org/10.5281/zenodo.10092585). This includes shell scripts for the classification and rasterization of point cloud data collected by a UAV laser scanning (ULS) system. The Zenodo folder also includes visualizations of flight paths for each survey and data comparisons made at the BURW, COPJ and NINE sites along the

Eastern Denali fault that were not included within the publication, as well as ULS point cloud cross sections that showcase stereotypical vegetation for each case study. All drone lidar data are available on the OpenTopography portal at the following links: XELF (https://doi.org/10.5069/G92V2DBC), SJF (https://doi.org/10.5069/G9TB1542), SRMT (https://doi.org/10.5069/G9PK0DCW), EDF (https://doi.org/10.5069/G998857Q). Airborne lidar data for the XELF (Section 3) and SRMT (Section 5) sites are available on the LidarBC (2023) portal.

Competing interests

The authors have no competing interests.

References

Arrowsmith, J. R., Rhodes, D. D., and Pollard, D. D. Morphologic dating of scarps formed by repeated slip events along the San Andreas Fault, Carrizo Plain, California. *Journal of Geophysical Research (Solid Earth)*, 103(B5):10,141–10,160, 1998. doi: 10.1029/98JB00505.

Baldwin, K., Allen, L., Basquill, S., Chapman, K., Downing, D., Flynn, N., MacKenzie, W., Major, M., Meades, W., Meidinger, D., Morneau, C., Saucier, J.-P., Thorpe, J., and Uhlig, P. Vegetation Zones of Canada: A Biogeoclimate Perspective, 2019.

Bemis, S. P., Micklethwaite, S., Turner, D., James, M. R., Akciz, S., Thiele, S. T., and Bangash, H. A. Ground-based and UAV-Based photogrammetry: A multi-scale, high-resolution mapping tool for structural geology and paleoseismology. *Journal of Structural Geology*, 69:163–178, 2014. doi: 10.1016/j.jsg.2014.10.007.

Benavente, C., Wimpenny, S., Rosell, L., Robert, X., Palomino, A., Audin, L., Aguirre, E., and García, B. Paleoseismic Evidence of an M_w 7 Pre-Hispanic Earthquake in the Peruvian Forearc. *Tectonics*, 40(6):e2020TC006479, 2021. doi: 10.1029/2020TC006479.

Bender, A. M. and Haeussler, P. J. Eastern Denali Fault surface trace map, eastern Alaska and Yukon, Canada. USGS Numbered Series 2017-1049, U.S. Geological Survey, Reston, VA, 2017.

Bertiger, W., Bar-Sever, Y., Dorsey, A., Haines, B., Harvey, N., Hemberger, D., Heflin, M., Lu, W., Miller, M., Moore, A. W., Murphy, D., Ries, P., Romans, L., Sibois, A., Sibthorpe, A., Szilagyi, B., Vallisneri, M., and Willis, P. GipsyX/RTGx, a new tool set for space geodetic operations and research. *Advances in Space Research*, 66(3):469–489, 2020. doi: 10.1016/j.asr.2020.04.015.

Blais-Stevens, A., Clague, J. J., Brahney, J., Lipovsky, P., Haeussler, P. J., and Menounos, B. Evidence for Large Holocene Earthquakes along the Denali Fault in Southwest Yukon, Canada. *Environmental & Engineering Geoscience*, 26(2):149–166, 2020. doi: 10.2113/EEG-2263.

Bostock, H. S. *Geology of northwest Shakwak Valley, Yukon Territory*. E. Cloutier, Queen's Printer, 1952.

Brandon, M. T. Origin of igneous rocks associated with melanges of the Pacific Rim Complex, western Vancouver Island, Canada. *Tectonics*, 8(6):1115–1136, 1989. doi: 10.1029/TC008i006p01115.

Brede, B., Lau, A., Bartholomeus, H. M., and Kooistra, L. Comparing RIEGL RiCOPTER UAV LiDAR Derived Canopy Height and DBH with Terrestrial LiDAR. *Sensors*, 17(10), 2017. doi: 10.3390/s17102371.

Brooks, B. A., Glennie, C., Hudnut, K. W., Ericksen, T., and Hauser, D. Mobile Laser Scanning Applied to the Earth Sciences. *Eos, Transactions American Geophysical Union*, 94(36):313–315, 2013. doi: 10.1002/2013EO360002.

Brooks, B. A., Minson, S. E., Glennie, C. L., Nevitt, J. M., Dawson, T., Rubin, R., Ericksen, T. L., Lockner, D., Hudnut, K., Langenheim, V., Lutz, A., Mareschal, M., Murray, J., Schwartz, D., and Zaccone, D. Buried shallow fault slip from the South Napa earthquake revealed by near-field geodesy. *Science Advances*, 3(7):e1700525, 2017. doi: 10.1126/sciadv.1700525.

Bubeck, A., Wilkinson, M., Roberts, G. P., Cowie, P. A., McCaffrey, K. J. W., Phillips, R., and Sammonds, P. The tectonic geomorphology of bedrock scarps on active normal faults in the Italian Apennines mapped using combined ground penetrating radar and terrestrial laser scanning. *Geomorphology*, 237:38–51, 2015. doi: 10.1016/j.geomorph.2014.03.011.

Butler, H., Chambers, B., Hartzell, P., and Glennie, C. PDAL: An open source library for the processing and analysis of point clouds. *Computers & Geosciences*, 148:104680, 2021. doi: 10.1016/j.cageo.2020.104680.

Chen, T., Akciz, S. O., Hudnut, K. W., Zhang, D. Z., and Stock, J. M. Fault-Slip Distribution of the 1999 Mw 7.1 Hector Mine Earthquake, California, Estimated from Postearthquake Airborne LiDAR Data. *Bulletin of the Seismological Society of America*, 105(2A):776–790, 2015. doi: 10.1785/0120130108.

Choi, M., Eaton, D. W., and Enkelmann, E. Is the Eastern Denali fault still active? *Geology*, 49(6):662–666, 2021. doi: 10.1130/G48461.1.

Civil Aviation Safety Authority. Remote pilot licence, Mar. 2021. https://www.casa.gov.au/drones/get-your-operator-credentials/remote-pilot-licence. https://www.casa.gov.au/drones/get-your-operator-credentials/remote-pilot-licence.

Clague, J. J. Late Quaternary Sediments and Geomorphic History of the Southern Rocky Mountain Trench, British Columbia. *Canadian Journal of Earth Sciences*, 12(4):595–605, 1975. doi: 10.1139/e75-054.

Clark, K. J., Nissen, E. K., Howarth, J. D., Hamling, I. J., Mountjoy, J. J., Ries, W. F., Jones, K., Goldstien, S., Cochran, U. A., Villamor, P., Hreinsdóttir, S., Litchfield, N. J., Mueller, C., Berryman, K. R., and Strong, D. T. Highly variable coastal deformation in the 2016 M_W7.8 Kaikōura earthquake reflects rupture complexity along a transpressional plate boundary. *Earth and Planetary Science Letters*, 474:334–344, 2017. doi: 10.1016/j.epsl.2017.06.048.

Cui, Y., Miller, D., Schiarizza, P., and Diakow, L. British Columbia digital geology. *British Columbia Ministry of Energy, Mines and Petroleum Resources, British Columbia Geological Survey Open File*, 8(9), 2017.

Cunningham, D., Grebby, S., Tansey, K., Gosar, A., and Kastelic, V. Application of airborne LiDAR to mapping seismogenic faults in forested mountainous terrain, southeastern Alps, Slovenia. *Geophysical Research Letters*, 33(20):L20308, 2006. doi: 10.1029/2006GL027014.

Căţeanu, M., Arcadie, C., and others. ALS for terrain mapping in forest environments: An analysis of LiDAR filtering algorithms. *EARSeL eProceedings*, 16(1):9–20, 2017. doi: 10.12760/01-2017-1-02.

DeLong, S. B., Lienkaemper, J. J., Pickering, A. J., and Avdievitch, N. N. Rates and patterns of surface deformation from laser scanning following the South Napa earthquake, California. *Geosphere*, 11(6):2015–2030, 2015. doi: 10.1130/GES01189.1.

Diederichs, A., Nissen, E. K., Lajoie, L. J., Langridge, R. M., Malireddi, S. R., Clark, K. J., Hamling, I. J., and Tagliasacchi, A. Unusual kinematics of the Papatea fault (2016 Kaikōura earthquake) suggest anelastic rupture. *Science Advances*, 5(10):eaax5703, 2019. doi: 10.1126/sciadv.aax5703.

DiFrancesco, P.-M., Bonneau, D., and Hutchinson, D. J. The implications of M3C2 projection diameter on 3D semi-automated rockfall extraction from sequential terrestrial laser scanning point clouds. *Remote Sensing*, 12(11):1885, 2020. doi: 10.3390/rs12111885.

DuRoss, C. B., Bunds, M. P., Gold, R. D., Briggs, R. W., Reitman, N. G., Personius, S. F., and Toké, N. A. Variable normal-fault rupture behavior, northern Lost River fault zone, Idaho, USA. *Geosphere*, 15(6):1869–1892, 2019. doi: 10.1130/GES02096.1.

Eberhart-Phillips, D., Haeussler, P. J., Freymueller, J. T., Frankel, A. D., Rubin, C. M., Craw, P., Ratchkovski, N. A., Anderson, G., Carver, G. A., Crone, A. J., Dawson, T. E., Fletcher, H., Hansen, R., Harp, E. L., Harris, R. A., Hill, D. P., Hreinsdóttir, S., Jibson, R. W., Jones, L. M., Kayen, R., Keefer, D. K., Larsen, C. F., Moran, S. C., Personius, S. F., Plafker, G., Sherrod, B., Sieh, K., Sitar, N., and Wallace, W. K. The 2002 Denali Fault Earthquake, Alaska: A Large Magnitude, Slip-Partitioned Event. *Science*, 300(5622): 1113–1118, 2003. doi: 10.1126/science.1082703.

Elliott, J., Nissen, E., England, P., Jackson, J. A., Lamb, S., Li, Z., Oehlers, M., and Parsons, B. Slip in the 2010–2011 Canterbury earthquakes, New Zealand. *Journal of Geophysical Research: Solid Earth*, 117(B3), 2012. doi: 10.1029/2011JB008868.

England, T. and Calon, T. The Cowichan fold and thrust system, Vancouver Island, southwestern British Columbia. *Geological Society of America Bulletin*, 103(3):336–362, 1991. doi: 10.1130/0016-7606(1991)103<0336:TCFATS>2.3.CO;2.

Esri. Ocean Basemap, 2022. https://www.arcgis.com/home/item.html?id=6348e67824504fc9a62976434bf0d8d5. https://www.arcgis.com/home/item.html?id=6348e67824504fc9a62976434bf0d8d5, (December 1, 2023).

European Union Aviation Safety Authority. Drones - National Aviation Authorities, 2022. https://www.easa.europa.eu/en/domains/civil-drones/naa. https://www.easa.europa.eu/en/domains/civil-drones/naa.

Federal Aviation Administration. Become a Drone Pilot, 2023. https://www.faa.gov/uas/commercial_operators/become_a_drone_pilot. https://www.faa.gov/uas/commercial_operators/become_a_drone_pilot.

Fernandez-Diaz, J., Carter, W., Shrestha, R., and Glennie, C. Now You See It… Now You Don't: Understanding Airborne Mapping LiDAR Collection and Data Product Generation for Archaeological Research in Mesoamerica. *Remote Sensing*, 6(10): 9951–10001, 2014. doi: 10.3390/rs6109951.

Finley, T., Salomon, G., Stephen, R., Nissen, E., Cassidy, J., and Menounos, B. Preliminary results and structural interpretations from drone LiDAR surveys over the Eastern Denali fault, Yukon. In *Yukon Exploration and Geology*, pages 83–105, 2022a.

Finley, T. D., Johnston, S. T., Unsworth, M. J., Banks, J., and Pana, D.-I. Modern dextral strain controls active hydrothermal systems in the southeastern Canadian Cordillera. *GSA Bulletin*, 2022b. doi: 10.1130/B36500.1.

Gabrielse, H., Monger, J., Wheeler, J., and Yorath, C. Morphogeological Belts, Tectonic Assemblages and Terranes, Chapter 2, Part A, of Geology of the Cordilleran Orogen in Canada, Geology of Canada, no. 4. *Geological Survey of Canada*, pages 15–28, 1991. doi: 10.4095/134073.

GDAL/OGR contributors. *GDAL/OGR Geospatial Data Abstraction software Library*. Open Source Geospatial Foundation, 2023. doi: 10.5281/zenodo.5884351.

Glennie, C., Brooks, B., Ericksen, T., Hauser, D., Hudnut, K., Foster, J., and Avery, J. Compact Multipurpose Mobile Laser Scanning System — Initial Tests and Results. *Remote Sensing*, 5(2): 521–538, 2013. doi: 10.3390/rs5020521.

Glennie, C. L., Carter, W. E., Shrestha, R. L., and Dietrich, W. E. Geodetic imaging with airborne LiDAR: the Earth's surface revealed. *Reports on Progress in Physics*, 76(8):086801, 2013. doi: 10.1088/0034-4885/76/8/086801.

Glennie, C. L., Hinojosa-Corona, A., Nissen, E., Kusari, A., Oskin, M. E., Arrowsmith, J. R., and Borsa, A. Optimization of legacy lidar data sets for measuring near-field earthquake displacements. *Geophysical Research Letters*, 41(10):3494–3501, 2014. doi: 10.1002/2014GL059919.

Gold, P. O., Oskin, M. E., Elliott, A. J., Hinojosa-Corona, A., Taylor, M. H., Kreylos, O., and Cowgill, E. Coseismic slip variation assessed from terrestrial lidar scans of the El Mayor-Cucapah surface rupture. *Earth and Planetary Science Letters*, 366:151–162, 2013. doi: 10.1016/j.epsl.2013.01.040.

Gu, Y., Xiao, Z., and Li, X. A Spatial Alignment Method for UAV LiDAR Strip Adjustment in Nonurban Scenes. *IEEE Transactions on Geoscience and Remote Sensing*, 61:1–13, 2023. doi: 10.1109/TGRS.2023.3281692.

Haddad, D. E., Akciz, S. O., Arrowsmith, J. R., Rhodes, D. D., Oldow, J. S., Zielke, O., Toke, N. A., Haddad, A. G., Mauer, J., and Shilpakar, P. Applications of airborne and terrestrial laser scanning to paleoseismology. *Geosphere*, 8(4):771–786, 2012. doi: 10.1130/GES00701.1.

Haeussler, P. J., Matmon, A., Schwartz, D. P., and Seitz, G. G. Neotectonics of interior Alaska and the late Quaternary slip rate along the Denali fault system. *Geosphere*, 13(5):1445–1463, 2017. doi: 10.1130/GES01447.1.

Harrichhausen, N., Morell, K. D., Regalla, C., Bennett, S. E., Leonard, L. J., Lynch, E. M., and Nissen, E. Paleoseismic trenching reveals Late Quaternary kinematics of the Leech River fault: Implications for forearc strain accumulation in northern Cascadia. *Bulletin of the Seismological Society of America*, 111(2): 1110–1138, 2021. doi: 10.1785/0120200204.

Harrichhausen, N., Morell, K. D., Regalla, C., Lynch, E. M., and Leonard, L. J. Eocene Terrane Accretion in Northern Cascadia Recorded by Brittle Left-Lateral Slip on the San Juan Fault. *Tectonics*, 41(10):e2022TC007317, 2022. doi: 10.1029/2022TC007317.

Harrichhausen, N., Finley, T., Morell, K. D., Regalla, C., Bennett, S. E. K., Leonard, L. J., Nissen, E., McLeod, E., Lynch, E. M., Salomon, G., and Sethanant, I. Discovery of an Active Forearc Fault in an Urban Region: Holocene Rupture on the XEOLXELEK-Elk Lake Fault, Victoria, British Columbia, Canada. *Tectonics*, 42 (12):e2023TC008170, 2023. doi: 10.1029/2023TC008170.

Harris Aerial. Carrier H6 Hybrid - Heavy Lift Drones, July 2023. https://harrisaerial.com/carrier-drones/carrier-h6-hybrid/.

Harwin, S. and Lucieer, A. Assessing the Accuracy of Georeferenced Point Clouds Produced via Multi-View Stereopsis from Unmanned Aerial Vehicle (UAV) Imagery. *Remote Sensing*, 4(6): 1573–1599, 2012. doi: 10.3390/rs4061573.

Haugerud, R. A., Harding, D. J., Johnson, S. Y., Harless, J. L., Weaver, C. S., and Sherrod, B. L. High-resolution lidar topography of the Puget Lowland, Washington. *GSA Today*, 13(6):4–10, 2003. doi: 10.1130/1052-5173(2003)13<0004:HLTOTP>2.0.CO;2.

Hilley, G. E., DeLong, S., Prentice, C., Blisniuk, K., and Arrowsmith, J. Morphologic dating of fault scarps using airborne laser swath mapping (ALSM) data. *Geophysical Research Letters*, 37 (4):L04301, 2010. doi: 10.1029/2009GL042044.

Hodge, M., Biggs, J., Fagereng, Å., Elliott, A., Mdala, H., and Mphepo, F. A semi-automated algorithm to quantify scarp morphology (SPARTA): application to normal faults in southern Malawi. *Solid Earth*, 10(1):27–57, 2019. doi: 10.5194/se-10-27-2019.

Hodgson, M. E. and Bresnahan, P. Accuracy of airborne lidar-derived elevation. *Photogrammetric Engineering & Remote Sensing*, 70(3):331–339, 2004. doi: 10.14358/pers.70.3.331.

Hubbard, T. D., Koehler, R. D., and Combellick, R. A. High-resolution lidar data for Alaska infrastructure corridors. *Alaska*

Division of Geological and Geophysical Surveys: Fairbanks, AK, USA, 3:291, 2011.

Hunter, L. E., Howle, J. F., Rose, R. S., and Bawden, G. W. LiDAR-Assisted Identification of an Active Fault near Truckee, California. *Bulletin of the Seismological Society of America*, 101(3): 1162–1181, 2011. doi: 10.1785/0120090261.

Isenburg, M. LAStools-efficient LiDAR processing software (version 210418), obtained from https://lastools.github.io/, 2021.

Ishimura, D., Toda, S., Mukoyama, S., Homma, S., Yamaguchi, K., and Takahashi, N. 3D Surface Displacement and Surface Ruptures Associated with the 2014 Mw 6.2 Nagano Earthquake Using Differential Lidar. *Bulletin of the Seismological Society of America*, 109(2):780–796, 2019. doi: 10.1785/0120180020.

James, M. R. and Robson, S. Straightforward reconstruction of 3D surfaces and topography with a camera: Accuracy and geoscience application. *Journal of Geophysical Research: Earth Surface*, 117(F3):F03017, 2012. doi: 10.1029/2011JF002289.

Johnson, K., Nissen, E., Saripalli, S., Arrowsmith, J. R., McGarey, P., Scharer, K., Williams, P., and Blisniuk, K. Rapid mapping of ultrafine fault zone topography with structure from motion. *Geosphere*, 10(5):969–986, 2014. doi: 10.1130/GES01017.1.

Johnson, K. L., Nissen, E., and Lajoie, L. Surface Rupture Morphology and Vertical Slip Distribution of the 1959 M_w 7.2 Hebgen Lake (Montana) Earthquake From Airborne Lidar Topography. *Journal of Geophysical Research (Solid Earth)*, 123(9): 8229–8248, 2018. doi: 10.1029/2017JB015039.

Johnson, S. Y. Evidence for a margin-truncating transcurrent fault (pre-late Eocene) in western Washington. *Geology*, 12(9):538–541, 1984. doi: 10.1130/0091-7613(1984)12<538:EFAMTF>2.0.CO;2.

Jones, R. R., Kokkalas, S., and McCaffrey, K. J. W. Quantitative analysis and visualization of nonplanar fault surfaces using terrestrial laser scanning (LIDAR)–The Arkitsa fault, central Greece, as a case study. *Geosphere*, 5(6):465–482, 2009. doi: 10.1130/GES00216.1.

Kellner, J. R., Armston, J., Birrer, M., Cushman, K. C., Duncanson, L., Eck, C., Falleger, C., Imbach, B., Král, K., Krůček, M., Trochta, J., Vrška, T., and Zgraggen, C. New Opportunities for Forest Remote Sensing Through Ultra-High-Density Drone Lidar. *Surveys in Geophysics*, 40(4):959–977, 2019. doi: 10.1007/s10712-019-09529-9.

Kolaj, M., Adams, J., and Halchuk, S. The 6th generation seismic hazard model of Canada. *Geological Survey of Canada, Open File 8630*, pages 1–12, 2020. doi: https://doi.org/10.4095/327322.

Lague, D., Brodu, N., and Leroux, J. Accurate 3D comparison of complex topography with terrestrial laser scanner: Application to the Rangitikei canyon (N-Z). *ISPRS Journal of Photogrammetry and Remote Sensing*, 82:10–26, 2013. doi: 10.1016/j.isprsjprs.2013.04.009.

Lajoie, L. J., Nissen, E., Johnson, K. L., Arrowsmith, J. R., Glennie, C. L., Hinojosa-Corona, A., and Oskin, M. E. Extent of Low-Angle Normal Slip in the 2010 El Mayor-Cucapah (Mexico) Earthquake From Differential Lidar. *Journal of Geophysical Research (Solid Earth)*, 124(1):943–956, 2019. doi: 10.1029/2018JB016828.

Langridge, R. M., Ries, W. F., Farrier, T., Barth, N. C., Khajavi, N., and De Pascale, G. P. Developing sub 5-m LiDAR DEMs for forested sections of the Alpine and Hope faults, South Island, New Zealand: Implications for structural interpretations. *Journal of Structural Geology*, 64:53–66, 2014. doi: 10.1016/j.jsg.2013.11.007.

Leandro, R. F., Santos, M. C., and Langley, R. B. Analyzing GNSS data in precise point positioning software. *GPS Solutions*, 15(1): 1–13, 2011. doi: 10.1007/s10291-010-0173-9.

Liang, Y., Zhao, C.-Z., Yuan, H., Chen, Y., Zhang, W., Huang, J.-Q., Yu, D., Liu, Y., Titirici, M.-M., Chueh, Y.-L., Yu, H., and Zhang, Q. A review of rechargeable batteries for portable electronic devices. *InfoMat*, 1(1):6–32, 2019. doi: 10.1002/inf2.12000.

LidarBC. Open LiDAR Data Portal, 2023. https://lidar.gov.bc.ca/.

Lin, Z., Kaneda, H., Mukoyama, S., Asada, N., and Chiba, T. Detection of subtle tectonic–geomorphic features in densely forested mountains by very high-resolution airborne LiDAR survey. *Geomorphology*, 182:104–115, 2013. doi: 10.1016/j.geomorph.2012.11.001.

Marechal, A., Ritz, J.-F., Ferry, M., Mazzotti, S., Blard, P.-H., Braucher, R., and Saint-Carlier, D. Active tectonics around the Yakutat indentor: New geomorphological constraints on the eastern Denali, Totschunda and Duke River Faults. *Earth and Planetary Science Letters*, 482:71–80, 2018. doi: 10.1016/j.epsl.2017.10.051.

Meigs, A. Active tectonics and the LiDAR revolution. *Lithosphere*, 5 (2):226–229, 2013. doi: 10.1130/RF.L004.1.

Metcalf, A., Welles, T., Murakami, Y., Nakamura, H., and Ahn, J. Unmanned Aerial Vehicle Solid Oxide Fuel Cell and Internal Combustion Engine Hybrid Powertrain: An Experimental and Simulation Centered Review. *American Society of Mechanical Engineers Digital Collection*, 2022. doi: 10.1115/POWER2022-86357.

Morell, K. D., Regalla, C., Leonard, L. J., Amos, C., and Levson, V. Quaternary rupture of a crustal fault beneath Victoria, British Columbia, Canada. *GSA Today*, 7(3), 2017. doi: 10.1130/GSATG291A.1.

Morin, P., Porter, C., Cloutier, M., Howat, I., Noh, M.-J., Willis, M., Bates, B., Willamson, C., and Peterman, K. ArcticDEM; A Publically Available, High Resolution Elevation Model of the Arctic. In *EGU General Assembly Conference Abstracts*, pages EPSC2016–8396, 2016.

Nash, D. B. Morphologic Dating of Degraded Normal Fault Scarps. *Journal of Geology*, 88(3):353–360, 1980. doi: 10.1086/628513.

Nelson, A. R., Personius, S. F., Wells, R. E., Schermer, E. R., Bradley, L., Buck, J., and Reitman, N. Holocene Earthquakes of Magnitude 7 during Westward Escape of the Olympic Mountains, Washington. *Bulletin of the Seismological Society of America*, 107 (5):2394–2415, 2017. doi: 10.1785/0120160323.

Nevitt, J. M., Brooks, B. A., Catchings, R. D., Goldman, M. R., Ericksen, T. L., and Glennie, C. L. Mechanics of near-field deformation during co- and post-seismic shallow fault slip. *Scientific Reports*, 10:5031, 2020. doi: 10.1038/s41598-020-61400-9.

Nissen, E., Maruyama, T., Ramon Arrowsmith, J., Elliott, J. R., Krishnan, A. K., Oskin, M. E., and Saripalli, S. Coseismic fault zone deformation revealed with differential lidar: Examples from Japanese $M_w \sim 7$ intraplate earthquakes. *Earth and Planetary Science Letters*, 405:244–256, 2014. doi: 10.1016/j.epsl.2014.08.031.

Oskin, M. E., Arrowsmith, J. R., Corona, A. H., Elliott, A. J., Fletcher, J. M., Fielding, E. J., Gold, P. O., Garcia, J. J. G., Hudnut, K. W., Liu-Zeng, J., and Teran, O. J. Near-Field Deformation from the El Mayor-Cucapah Earthquake Revealed by Differential LIDAR. *Science*, 335(6069):702, 2012. doi: 10.1126/science.1213778.

Pellicani, R., Argentiero, I., Manzari, P., Spilotro, G., Marzo, C., Ermini, R., and Apollonio, C. UAV and Airborne LiDAR Data for Interpreting Kinematic Evolution of Landslide Movements: The Case Study of the Montescaglioso Landslide (Southern Italy). *Geosciences*, 9(6):248, 2019. doi: 10.3390/geosciences9060248.

Pingel, T. J., Clarke, K. C., and McBride, W. A. An improved simple morphological filter for the terrain classification of airborne LIDAR data. *ISPRS Journal of Photogrammetry and Remote Sensing*, 77:21–30, 2013. doi: 10.1016/j.isprsjprs.2012.12.002.

Piriz, R., Mozo, A., Navarro, P., and Rodriguez, D. MagicGNSS: Precise GNSS products out of the box. In *Proceedings of the 21st International Technical Meeting of the Satellite Division of The Institute of Navigation (ION GNSS 2008)*, pages 1242–1251, 2008.

Prentice, C. S., Crosby, C. J., Whitehill, C. S., Arrowsmith, J. R., Furlong, K. P., and Phillips, D. A. Illuminating Northern California's Active Faults. *EOS Transactions*, 90(7):55, 2009. doi: 10.1029/2009EO070002.

Purba, J. C. S., Gilbert, H., and Dettmer, J. Structure and Dynamics of the Southern Rocky Mountain Trench near Valemount, British Columbia, Inferred from Local Seismicity. *Seismological Research Letters*, 92(5):3087–3099, 2021. doi: 10.1785/0220200350.

Rajashekara, K. Present Status and Future Trends in Electric Vehicle Propulsion Technologies. *IEEE Journal of Emerging and Selected Topics in Power Electronics*, 1(1):3–10, 2013. doi: 10.1109/JESTPE.2013.2259614.

Resop, J. P., Lehmann, L., and Hession, W. C. Drone laser scanning for modeling riverscape topography and vegetation: Comparison with traditional aerial lidar. *Drones*, 3(2):35, 2019. doi: 10.3390/drones3020035.

Risbøl, O. and Gustavsen, L. LiDAR from drones employed for mapping archaeology–Potential, benefits and challenges. *Archaeological Prospection*, 25(4):329–338, 2018. doi: 10.1002/arp.1712.

Ristau, J., Rogers, G. C., and Cassidy, J. F. Stress in western Canada from regional moment tensor analysis. *Canadian Journal of Earth Sciences*, 44(2):127–148, 2007. doi: 10.1139/e06-057.

Rusmore, M. E. and Cowan, D. S. Jurassic–Cretaceous rock units along the southern edge of the Wrangellia terrane on Vancouver Island. *Canadian Journal of Earth Sciences*, 22(8):1223–1232, 1985. doi: 10.1139/e85-124.

Salisbury, J. B., Rockwell, T. K., Middleton, T. J., and Hudnut, K. W. LiDAR and Field Observations of Slip Distribution for the Most Recent Surface Ruptures along the Central San Jacinto Fault. *Bulletin of the Seismological Society of America*, 102(2):598–619, 2012. doi: 10.1785/0120110068.

Salomon, G. W., New, T., Muir, R. A., Whitehead, B., Scheiber-Enslin, S., Smit, J., Stevens, V., Kahle, B., Kahle, R., Eckardt, F. D., and Alastair Sloan, R. Geomorphological and geophysical analyses of the Hebron Fault, SW Namibia: implications for stable continental region seismic hazard. *Geophysical Journal International*, 229(1):235–254, 2022. doi: 10.1093/gji/ggab466.

Sawicki, O. and Smith, D. G. Glacial Lake Invermere, upper Columbia River valley, British Columbia: a paleogeographic reconstruction. *Canadian Journal of Earth Sciences*, 29(4): 687–692, 1992. doi: 10.1139/e92-059.

Schermer, E. R., Amos, C. B., Duckworth, W. C., Nelson, A. R., Angster, S., Delano, J., and Sherrod, B. L. Postglacial Mw 7.0-7.5 Earthquakes on the North Olympic Fault Zone, Washington. *Bulletin of the Seismological Society of America*, 111(1):490–513, 2021. doi: 10.1785/0120200176.

Scott, C., Phan, M., Nandigam, V., Crosby, C., and Arrowsmith, J. R. Measuring change at Earth's surface: On-demand vertical and three-dimensional topographic differencing implemented in OpenTopography. *Geosphere*, 17(4):1318–1332, 2021. doi: 10.1130/GES02259.1.

Scott, C. P., Arrowsmith, J. R., Nissen, E., Lajoie, L., Maruyama, T., and Chiba, T. The M7 2016 Kumamoto, Japan, Earthquake: 3-D Deformation Along the Fault and Within the Damage Zone Constrained From Differential Lidar Topography. *Journal of Geophysical Research (Solid Earth)*, 123(7):6138–6155, 2018. doi: 10.1029/2018JB015581.

Scott, C. P., DeLong, S. B., and Arrowsmith, J. R. Distribution of Aseismic Deformation Along the Central San Andreas and Calaveras Faults From Differencing Repeat Airborne Lidar. *Geophysical Research Letters*, 47(22):e90628, 2020. doi: 10.1029/2020GL090628.

Scott, C. P., Beckley, M., Phan, M., Zawacki, E., Crosby, C., Nandigam, V., and Arrowsmith, R. Statewide USGS 3DEP Lidar Topographic Differencing Applied to Indiana, USA. *Remote Sensing*, 14(4):847, 2022. doi: 10.3390/rs14040847.

Skyfront. Perimeter 8 UAS, 2023. https://skyfront.com/perimeter-8. https://skyfront.com/perimeter-8.

Stöcker, C., Bennett, R., Nex, F., Gerke, M., and Zevenbergen, J. Review of the Current State of UAV Regulations. *Remote Sensing*, 9(5), 2017. doi: 10.3390/rs9050459.

Telling, J., Lyda, A., Hartzell, P., and Glennie, C. Review of Earth science research using terrestrial laser scanning. *Earth Science Reviews*, 169:35–68, 2017. doi: 10.1016/j.earscirev.2017.04.007.

Tomsett, C. and Leyland, J. Development and Testing of a UAV Laser Scanner and Multispectral Camera System for Eco-Geomorphic Applications. *Sensors*, 21(22):7719, 2021. doi: 10.3390/s21227719.

Toth, C., Brzezinska, D., Csanyi, N., Paska, E., and Yastikli, N. LiDAR mapping supporting earthquake research of the San Andreas fault. In *Proceedings of the ASPRS 2007 Annual Conference*, pages 1–11. American Society for Photogrammetry and Remote Sensing (ASPRS) Tampa, FL, 2007.

Townsend, A., Jiya, I. N., Martinson, C., Bessarabov, D., and Gouws, R. A comprehensive review of energy sources for unmanned aerial vehicles, their shortfalls and opportunities for improvements. *Heliyon*, 6(11):e05285, 2020. doi: 10.1016/j.heliyon.2020.e05285.

Transport Canada. Getting a drone pilot certificate, 2022. https://tc.canada.ca/en/aviation/drone-safety/drone-pilot-licensing/getting-drone-pilot-certificate. https://tc.canada.ca/en/aviation/drone-safety/drone-pilot-licensing/getting-drone-pilot-certificate.

Transport Canada. Minister of Transport announces Canada's first proposed drone safety regulations for beyond visual line-of-sight operations, 2023. https://www.canada.ca/en/transport-canada/news/2023/06/minister-of-transport-announces-canadas-first-proposed-drone-safety-regulations-for-beyond-visual-line-of-sight-operations.html. https://www.canada.ca/en/transport-canada/news/2023/06/minister-of-transport-announces-canadas-first-proposed-drone-safety-regulations-for-beyond-visual-line-of-sight-operations.html.

UK Civil Aviation Authority. Registering a drone or model aircraft, 2023. https://register-drones.caa.co.uk/individual. https://register-drones.caa.co.uk/individual.

van der Velden, A. J. and Cook, F. A. Structure and tectonic development of the southern Rocky Mountain trench. *Tectonics*, 15 (3):517–544, 1996. doi: 10.1029/95TC03288.

Van Tassel, C. Defining the true cost behind implementing lidar systems into your business., 2021. https://candrone.com/blogs/news/the-real-cost-of-starting-a-lidar-drone-business. https://candrone.com/blogs/news/the-real-cost-of-starting-a-lidar-drone-business.

VanValkenburgh, P., Cushman, K., Butters, L. J. C., Vega, C. R., Roberts, C. B., Kepler, C., and Kellner, J. Lasers without lost cities: Using drone lidar to capture architectural complexity at Kuelap, Amazonas, Peru. *Journal of Field Archaeology*, 45(sup1): S75–S88, 2020. doi: 10.1080/00934690.2020.1713287.

Viswanathan, V., Epstein, A. H., Chiang, Y.-M., Takeuchi, E., Bradley, M., Langford, J., and Winter, M. The challenges and opportunities of battery-powered flight. *Nature*, 601(7894):519–525, 2022. doi: 10.1038/s41586-021-04139-1.

Wang, S., Ren, Z., Wu, C., Lei, Q., Gong, W., Ou, Q., Zhang, H., Ren, G., and Li, C. DEM generation from Worldview-2 stereo imagery and vertical accuracy assessment for its application in active tectonics. *Geomorphology*, 336:107–118, 2019. doi: 10.1016/j.geomorph.2019.03.016.

Wedmore, L. N. J., Gregory, L. C., McCaffrey, K. J. W., Goodall, H., and Walters, R. J. Partitioned Off-Fault Deformation in the 2016 Norcia Earthquake Captured by Differential Terrestrial Laser Scanning. *Geophysical Research Letters*, 46(6):3199–3205, 2019. doi: 10.1029/2018GL080858.

Wei, Z., He, H., Su, P., Zhuang, Q., and Sun, W. Investigating paleoseismicity using fault scarp morphology of the Dushanzi Reverse Fault in the northern Tian Shan, China. *Geomorphology*, 327:542–553, 2019. doi: 10.1016/j.geomorph.2018.11.025.

Westoby, M., Brasington, J., Glasser, N., Hambrey, M., and Reynolds, J. 'Structure-from-Motion' photogrammetry: A low-cost, effective tool for geoscience applications. *Geomorphology*, 179:300–314, 2012. doi: 10.1016/j.geomorph.2012.08.021.

Wiatr, T., Reicherter, K., Papanikolaou, I., Fernández-Steeger, T., and Mason, J. Slip vector analysis with high resolution t-LiDAR scanning. *Tectonophysics*, 608:947–957, 2013. doi: 10.1016/j.tecto.2013.07.024.

Wieser, M., Hollaus, M., Mandlburger, G., Glira, P., and Pfeifer, N. ULS LiDAR supported analyses of laser beam penetration from different ALS systems into vegetation. *ISPRS Annals of Photogrammetry, Remote Sensing & Spatial Information Sciences*, 3 (3), 2016. doi: 10.5194/isprs-annals-III-3-233-2016.

Witter, R. C., Bender, A. M., Scharer, K. M., DuRoss, C. B., Haeussler, P. J., and Lease, R. O. Geomorphic expression and slip rate of the Fairweather fault, southeast Alaska, and evidence for predecessors of the 1958 rupture. *Geosphere*, 17(3):711–738, 2021. doi: 10.1130/GES02299.1.

Xiaoye Liu. Airborne LiDAR for DEM generation: some critical issues. *Progress in Physical Geography: Earth and Environment*, 32(1):31–49, 2008. doi: 10.1177/0309133308089496.

Zhang, B., Liao, Y., Guo, S., Wallace, R. E., Bucknam, R. C., and Hanks, T. C. Fault scarps related to the 1739 earthquake and seismicity of the Yinchuan graben, Ningxia Huizu Zizhiqu, China. *Bulletin of the Seismological Society of America*, 76(5): 1253–1287, 1986. doi: 10.1785/BSSA0760051253.

Zhang, K., Chen, S.-C., Whitman, D., Shyu, M.-L., Yan, J., and Zhang, C. A progressive morphological filter for removing nonground measurements from airborne LIDAR data. *IEEE Transactions on Geoscience and Remote Sensing*, 41(4):872–882, 2003. doi: 10.1109/TGRS.2003.810682.

Zhang, W., Qi, J., Wan, P., Wang, H., Xie, D., Wang, X., and Yan, G. An Easy-to-Use Airborne LiDAR Data Filtering Method Based on Cloth Simulation. *Remote Sensing*, 8(6), 2016. doi: 10.3390/rs8060501.

Zhu, X., Glennie, C. L., and Brooks, B. A. Automated near-field deformation detection from mobile laser scanning for the 2014 M_w 6.0 South Napa earthquake. *Journal of Applied Geodesy*, 16(1): 65–79, 2022. doi: 10.1515/jag-2021-0023.

Zielke, O., Arrowsmith, J. R., Ludwig, L. G., and Akçiz, S. O. Slip in the 1857 and Earlier Large Earthquakes Along the Carrizo Plain, San Andreas Fault. *Science*, 327(5969):1119–1122, 2010. doi: 10.1126/science.1182781.

Zielke, O., Klinger, Y., and Arrowsmith, J. R. Fault slip and earthquake recurrence along strike-slip faults - Contributions of high-resolution geomorphic data. *Tectonophysics*, 638:43–62, 2015. doi: 10.1016/j.tecto.2014.11.004.